Equations continues pour l'étude de la dynamique des écoulements granulaires denses hétèrogènes

Carolina Meruane

▶ **To cite this version:**

HAL Id: tel-00719232

https://theses.hal.science/tel-00719232

Submitted on 19 Jul 2012

N^o d'Orde: D.U. 2031

UNIVERSITE BLAISE PASCAL

U.F.R. Sciences et Technologies

ECOLE DOCTORALE DES SCIENCES FONDAMENTALES

N° 645

Université du Chili

Faculté des Sciences Physiques et Mathématiques

THESE

en cotutelle présentée pour obtenir le grade de

DOCTEUR D'UNIVERSITE

Spécialité: Volcanologie

Par **Carolina MERUANE**

Diplômée en Ingénierie Civile

EQUATIONS CONTINUES POUR L'ETUDE DE LA DYNAMIQUE DES ECOULEMENTS GRANULAIRES DENSES HETEROGENES

Soutenue publiquement le 02/06/2010, devant la commission d'examen.

Président: Rodrigo SOTO (Université du Chili)

Rapporteurs: Christophe ANCEY (Ecole Polytechnique Fédérale de Lausanne) et

Anne MANGENEY (Institut de Physique du Globe de Paris)

Examinateur: Jorge CLAVERO (Université du Chili)

Directeurs de thèse: Olivier ROCHE (Université Blaise Pascal) et

Aldo TAMBURRINO (Université du Chili)

Résumé

La plupart des écoulements granulaires denses dans la nature, tels que les avalanches de débris, les écoulements pyroclastiques, les glissements de terrain et les avalanches sous-marines, sont constitués d'un large éventail de différents composants solides immergés dans un environnement fluide. Afin d'obtenir une bonne représentation de la dynamique de ces écoulements, il est nécessaire d'examiner les mécanismes d'interaction entre les différents composants du mélange. Dans ce travail, nous avons développé un cadre théorique basé sur la théorie de mélange afin de représenter la dynamique d'un écoulement dense de matériau granulaire hétérogène composé d'un certain nombre d'espèces solides avec des propriétés différentes, et immergé dans un environnement fluide Newtonien. Le système d'équations obtenu a été validé en comparant les résultats numériques avec des mesures expérimentales obtenues pour des écoulements gravitaires de matériaux granulaires, générés par l'effondrement d'une colonne de grains en deux dimensions, en utilisant de l'air ou de l'eau comme milieu fluide. Cette théorie a ensuite été utilisée pour étudier les effets du fluide ambiant sur la dynamique des écoulements de matériaux granulaires homogènes, ainsi que les effets de la ségrégation sur la dynamique des écoulements granulaires de mélanges binaires constitués de petites et grandes particules sphériques d'égale densité. Nos résultats suggèrent que les équations reproduisent les caractéristiques essentielles de la dynamique des écoulements granulaires denses hétérogènes. En particulier, nous montrons que le fluide ambiant modifie la dynamique de l'écoulement granulaire via des changements de la pression hydrodynamique et des interactions de frottement entre le fluide et les particules solides. D'une part, la pression hydrodynamique du fluide peut supporter le poids apparent des particules, induisant ainsi une transition entre un écoulement granulaire dense compactée et un écoulement granulaire dense en suspension. D'autre part, les forces de frottement s'opposent au mouvement des particules, en particulier près des bords. En outre, nous démontrons que la ségrégation des matériaux granulaires augmente la vitesse du front en raison de la dilatation de l'écoulement. Cette augmentation de la vitesse d'écoulement est amortie par l'environnement fluide, et ce comportement est plus marqué dans l'eau que dans l'air. Par conséquent, la vitesse réelle du front est le résultat de l'équilibre entre l'expansion volumétrique causée par la ségrégation et la force de frottement imposée par le milieu fluide. Sur la base des résultats de cette étude, nous concluons qu'un modèle réaliste pour des écoulements granulaires hétérogènes doit considérer au moins trois éléments: des grains de petite et de grande taille et un environnement fluide. Ainsi, le cadre théorique proposé dans cette thèse peut être utile pour étudier la dynamique grande échelle des écoulements géophysiques dans la nature. Les principaux résultats de cette thèse ont fait l'objet de deux articles, le premier publié dans Journal of Fluid Mechanics (2010, **648**: 381 - 404), et le second soumis au même journal.

Summary

Most dense grains flows in nature, such as debris avalanches, pyroclastic flows, landslides and subaquatic avalanches, involve a wide range of different solid constituents that are immersed in an ambient fluid. In order to obtain a good representation of these flows, the interaction mechanisms among the different constituents of the mixture should be considered. In this research, it was developed a theoretical framework based on the mixture theory for representing the dynamics of a dense heterogeneous granular flow composed by a number of solid species with different properties, and immersed in a Newtonian ambient fluid. These fully coupled equations were solved numerically and validated by comparing the numerical results with experimental measurements of gravitational granular flows, triggered by the collapse of two-dimensional granular columns in ambient air or water. This theory was then used to investigate the ambient fluid effects on homogeneous granular flow dynamics, and the segregation effects on the dynamics of binary mixtures of small and large spherical particles of equal mass density. Our results suggest that the model equations include the essential features that describe the dynamics of dense heterogeneous granular flows. In particular, it is shown that the ambient fluid modifies the granular flow dynamics via hydrodynamic fluid pressure and drag interactions between the fluid and the solids. On the one hand, hydrodynamic fluid pressure can hold the reduced weight of the solids, thus inducing a transition from dense-compacted to dense-suspended granular flows. On the other hand, drag forces counteract the solids movement, especially within the near-wall viscous layer. Furthermore, it is shown that segregation of the granular material increases the front speed because of the volumetric expansion of the flow. This increase in flow speed is damped by the ambient fluid, and this behaviour is more pronounced in water compared to the case in air. Therefore, the actual front speed is the result of the balance between the volumetric expansion caused by segregation and the drag force imposed by the ambient fluid. Based on the results of this thesis, it is concluded that a realistic model of dense heterogeneous granular flows should consider at least three constituents: large and small grains, and the ambient fluid. So that, the continuum framework proposed here may be useful to study the large scale dynamics of these kinds of flows in nature, such as geophysical flows. The main results of this thesis were published in two scientific articles, the first one in the Journal of Fluid Mechanics (2010, **648**: 381 - 404), and the second one submitted to the same journal.

A mis padres Bibiana y Teodoro

Acknowledgments

Contents

Chapter 1

Introduction

1.1. Approaches to model granular flows

A granular flow is a collection of discrete solid particles that in motion behaves like a fluid (Campbell 2006). These flows are common in numerous industrial and environmental contexts. In the latter case, landslides, debris avalanches and pyroclastic flows represent important natural hazards (Forterre & Pouliquen 2008). In general, granular flows in nature are composed of various particle types that differ in size, shape, density, and roughness, and the spaces between the particles are filled with a lighter fluid, usually water or air (Ancey 2007). As the dynamics of these flows involve different aspects of fluid mechanics, plasticity theory, solid mechanics and rheology (Wang & Hutter 2001), the combination of experimental and theoretical studies, as well as field observations and numerical simulations, is often required for their understanding (Ancey 2007). Although in specific cases our knowledge of the dynamics of granular flows has greatly improved (Goldhirsch 2003), so far no widely accepted set of governing equations exists.

The dynamics of granular flows has been commonly represented using two different approaches: the discrete element approach (Cundall & Strack 1979) and the continuum approach (Goldhirsch 2003; Hutter *et al.* 2005). In the first approach, each grain is modelled by using the standard equations of motion that describe its kinematics (Cundall & Strack 1979), and the interactions between the grains are represented by contact laws models (Moreau 1994). In the second approach, the granular material is represented as a continuum, for which two different approaches are used depending on the granular flow regime. On the one hand, the dilute and rapid granular flow regime is represented in a way similar to the thermal motion of molecules in the kinetic theory of gases, but also considering the energy loss due to inelastic collisions (Campbell 1990; Goldhirsch 2003). On the other hand, the dense quasi-static regime is represented with the Mohr-Coulomb sliding condition, in which it is further assumed that the flow is incompressible, and the mass and momentum conservation equations are vertically averaged such as obtaining the so-called Savage-Hutter avalanche model (Hutter *et al.* 2005). Because of practical reasons of numerical efficacy, the discrete element approach has been limited to obtain information on the evolution of the internal microstructure of the granular flow under idealized conditions (e.g Staron & Hinch

2005), whereas the Savage-Hutter avalanche model has been used extensively for describing flows in complex geometry, as in the case of geophysical flows (e.g Savage & Huter 1989; Wieland *et al.* 1999; Hutter *et al.* 2005; Pudasaini *et al.* 2005). The advantage of the Savage-Hutter model is that the rheology of the granular material is included as a single term that describes the frictional stress with the substrate (Forterre & Pouliquen 2008). The disadvantage, however, is that the analysis is restricted to the case of a homogenous mixture, when the active layer is very thin compared to the horizontal dimensions and the role of ambient fluid is negligible (Hutter *et al.* 2005). Recently, more sophisticated approaches that consider the presence of the interstitial fluid have been developed (Iverson 1997; Iverson & Denlinger 2001; Pitman & Le 2005; Pelanti *et al.* 2008); however, the ambient fluid effects on the granular flow dynamics has not been investigated in detail.

The role of the ambient fluid can be investigated through a two-phase continuum model, considering the respective relationships that describe the interactions between the constituents (Drew 1983). Two different continuum theories can be followed: the mixture theory (Truesdell 1957) and the phase-averaged theory (Anderson & Jackson 1967). The mixture theory was formulated for studying the dynamics of mixtures of gases, through a generalisation of basis and principles of continuous mechanics. The key abstraction in this theory is that, at any time, every point in space is occupied simultaneously by one particle of each constituent (Truesdell 1984). In order to derive a similar approach for fluid-solid mixtures, immiscibility of the constituents was considered by introducing the volume fraction of the components as additional kinematic variables (e.g. Bedford 1983; Passman *et al.* 1984). On the other hand, the phase-averaged formulation is based on an average of the mass and momentum balance laws for fluid and solid constituents over time or volume (Anderson & Jackson 1967; Drew 1983). Even if both theories allow the study of the dynamics of fluid-solid mixtures, they give different representations of the constitutive relations (Joseph & Lundgren 1990). A major challenge is to unify both theories and obtain a unique set of governing equations.

Another important point that has not been deeply taken into account in the approaches described above is the heterogeneity of the granular material. Geophysical flows commonly involve a wide range of solid particle sizes that vary between micrometers to meters (Ancey 2007). As a consequence, granular flows in nature often exhibit a non-uniform spatial distribution of particles, which is the result of a combination of mechanisms associated to the nature of the flow and the properties of the constituents (Ottino & Khakhar 2000). For instance, granular avalanches are very efficient at sorting particles by size, in which the small particles percolate downwards and the large ones rise up to the free surface of the flow (Savage & Lun 1988). This configuration, called inverse gradient, has been obeserved in deposits of pyroplastics flows and de-

bris avalanches (e.g van Wyk de Vries *et al.* 2001; Wang & Hutter 2001; Clavero *et al.* 2002). This segregation mechanism may compete against the diffusive remixing mechanism that occurs in rapid avalanches (Dolgunin & Ukolov 1995; Gray & Chugunov 2006), or against the mass effect mechanism in case of large diameter ratios (Thomas 2000). Moreover, when the large particles are more angular and therefore more resistant to flow, segregation occurs simultaneously with fingering instability of the avalanche front (Pouliquen *et al.* 1997), or with spontaneous stratication in two-dimensional silos (Makse *et al.* 1997). Another notable feature of granular flows of binary mixtures is their high mobility, defined as the ratio of the runout distance to the fall height, compared to the cases involving only one grain size (Roche *et al.* 2005; Phillips *et al.* 2006; Linares-Gerrero *et al.* 2007). This may be caused by a thin layer of small particles at the base of the flow that changes the frictional dynamics from sliding to rolling (Phillips *et al.* 2006; Linares-Gerrero *et al.* 2007). Furthermore, the interactions between the particles and their ambient fluid may also have a role on the mixture flow dynamics. For instance, in case of binary mixtures of small and large particles, front fingering instability and inverse vertical segregation are damped in the presence of water (Pouliquen & Vallance 1999; Vallance & Savage 2000); and binary mixtures of bronze and glass beads of equal size exhibit an spontaneous separation under vertical vibration in the presence of air, with a bronze-rich and glass-rich layers forming a sandwich configuration (Burtally *et al.* 2002), which is the result of the interaction with the air flow that is induced by the vertical vibration of the container (Biswas *et al.* 2003).

The examples described above show that in order to obtain a good representation of dense heterogenous granular flows, the interaction mechanisms between the different constituents of the mixture should be considered. In this context, the mixture theory (Truesdell 1957, 1984) appears to be a useful tool for describing the dynamics of these flows. This idea has been recently followed by Gray & Thornton (2005), Gray & Chugunov (2006), and Thornton *et al.* (2006), who used the mixture theory to describe particle-size segregation and diffusive remixing in granular avalanches of two or three constituents. Their models consist of a single equation for the volume fraction of the smaller particles, and are closely related to the models proposed by Savage & Lun (1988) and Dolgunin & Ukolov (1995). Although these approaches are promising for predicting segregation in dense granular avalanches, at present days there is no empirical relations for the parameters introduced to describe the segregation and remixing fluxes, neither their dependence with the particles and flow properties (Gray & Chugunov 2006). In particular, these theories do not consider the feedback that exists between the particle-size distribution and the dynamics of the flow (Gray & Ancey 2009).

1.2. Purpose of this research

The main objective of this thesis was to develop a theoretical framework based on the continuum approach for representing the dynamics of a dense heterogeneous granular flow composed by a number of solid species with different properties (grain size, density and roughness), and immersed in a Newtonian ambient fluid. With this aim, two specific objectives were defined:

(a) To study the role of the ambient viscous fluid on the dynamics of gravitational granular flows. In this context, we proposed and validated a set of two-phase continuum equations for studying a granular flow composed of homogeneous solid particles and a Newtonian ambient fluid. With this set of governing equations, the role of the ambient viscous fluid on the dynamics of gravitational granular flows was analysed experimentally and numerically for the collapse and spreading of a two-dimensional granular column in air or water, for different solid particle sizes and column aspect (height to length) ratios. We chose this particular configuration because it has widely been studied, it is characterised by an unsteady behaviour with a transition between static and flowing states, and it represents an ideal case to validate the non-hydrostatic model (e.g. Balmforth & Kerswell 2005; Staron & Hinch 2005; Lube *et al.* 2005; Lajeunesse *et al.* 2005; Larrieu *et al.* 2006).

(b) To develop a continuum mixture theory for representing the dynamics of a dense heterogeneous granular flow composed of a number of species with different properties and immersed in a Newtonian ambient fluid. In this context, we extended the proposed two-phase approach to the case of dense heterogeneous mixtures of solid particles, by including in the momentum equations a constitutive relation that describes the interaction mechanisms between the solid constituents in a dense regime. Although these governing equations are general for any mixture of solid constituents in a dense regime, we focused on binary mixtures of small and large spherical particles of equal mass density. For this case, the dynamics of the granular flow was analysed experimentally and numerically for the collapse and spreading of two-dimensional granular columns in air or water, for different binary mixtures of solid particles and column height to length ratios.

To carry out the research needed to accomplish the declared objectives, a numerical code in FORTRAN 90 was developed to solve the fully coupled system of proposed equations, and laboratory experiments of gravitational granular flows triggered by the collapse of two-dimensional granular columns in ambient air or water were done.

1.3. Outline

This thesis is organised as follows. The derivation of the governing equations is detailed in Chapter 2, in which we first propose a set of two-phase continuum equations for studying a granular flow composed of homogeneous solid particles and immersed in a Newtonian ambient fluid, and then we extend the two-phase approach to the case of dense heterogeneous mixtures of solid particles. In Chapter 3, the experimental and numerical methods for the collapse and spreading of a two-dimensional granular column are described, and the dimensionless equations for this particular problem are detailed in Chapter 4. The results are presented in Chapter 5, in which the model equations are validated by comparing directly the numerical results with the experimental measurements using the front speed to describe the flow. Furthermore, it is shown in this chapter that the ambient fluid modifies the granular flow dynamics via hydrodynamic fluid pressure and drag interactions, and the segregation of the granular flow increases the front speed because of the volumetric expansion of the flow. Finally, in Chapter 6 we discuss the main results and show that a realistic model of dense heterogeneous granular flows should consider at least three constituents: large and small grains, and the ambient fluid.

The main results of this thesis were published in two scientific articles, the first one in the Journal of Fluid Mechanics (**2010**, **648**: 381 - 404), and the second one submitted to the same journal.

Chapter 2

Governing equations

2.1. Mixture theory framework

The mixture theory framework (Truesdell 1984) formulated for constituents with microstructure, is used here to obtain the governing equations for a dense granular flow consisting of an heterogeneous mixture of solid particles and a Newtonian ambient fluid. This framework is based on the mathematical theory formulated by Truesdell (1957) for studying the dynamics of mixtures of gases, in which the continuum description for each constituent was possible by assuming that, at any time, every point in space is occupied simultaneously by one particle of each constituent (Truesdell 1984). As this assumption is not valid in case of immiscible mixtures such as fluid-solids mixtures, in order to extend this theory to mixtures with microstructure, the immiscibility of the constituents was taken into account by introducing the volume fraction of the components as additional kinematic variables (e.g. Bedford 1983; Passman *et al.* 1984). This continuum description is only valid if the smaller dimension of the flow problem is larger than the dimension of a typical particle o pore (Passman *et al.* 1984).

Starting with this approach, we consider a mixture of *N+1* medium continuous, that is, it is assumed that all the space is filled simultaneously by particles of each constituent at any time *t*. In order to identify the components of the mixture, the sub-index $\alpha = 0$ and $\alpha = 1, 2, ..., N$ are used for fluid and solids constituents, respectively. The mixture occupies a reference volume V, which is large compared to the particles size, and the constituent α occupies a volume V_α within V, such as $V = \sum_\alpha V_\alpha$. Each constituent has a material density γ_α, a velocity $u_{\alpha i}$, and a volumetric concentration c_α. The partial density is defined as $\rho_\alpha \equiv c_\alpha \gamma_\alpha$.

Because there is no mass transfer between constituents, the mass and momentum conservation equations for each constituent are written as (Truesdell 1984)

$$\frac{\partial \rho_\alpha}{\partial t} + \frac{\partial (\rho_\alpha u_{\alpha i})}{\partial x_i} = 0, \tag{2.1}$$

$$\frac{\partial \rho_\alpha u_{\alpha i}}{\partial t} + \frac{\partial (\rho_\alpha u_{\alpha j} u_{\alpha i})}{\partial x_j} = \rho_\alpha f_{\alpha i} + \frac{\partial T_{\alpha ij}}{\partial x_j} + \hat{m}_{\alpha i}, \tag{2.2}$$

where $\rho_\alpha f_{\alpha i}$ represents the body forces acting on the constituent α in the *ith* direction;

$T_{\alpha ij}$ denotes the partial stress tensor of the constituent α; and $\hat{m}_{\alpha i}$ represents the interaction force between the constituent α and the other components of the mixture such as $\hat{m}_{\alpha i} = \sum_{\beta \neq \alpha} \hat{m}_{\beta \alpha i}$, with $\hat{m}_{\beta \alpha i} = -\hat{m}_{\alpha \beta i}$ being the reciprocal forces between the constituents β and α, and $\sum_{\alpha} \hat{m}_{\alpha i} = \sum_{\alpha} \sum_{\beta \neq \alpha} \hat{m}_{\beta \alpha i} = 0$.

Constitutive relations for the interaction force between the constituents, as well as the stress tensor for each constituent are required to close the mathematical system of equations formed by (2.1) and (2.2). By simplicity, a two-phase approach for homogeneous solid particles is analysed first, and then it is further extended to the case of dense heterogeneous mixtures of solid particles.

2.2. Compressible homogeneous granular flows

In this section, a two-phase approach for studying a compressible granular flow composed of homogeneous solid particles and immersed in a Newtonian ambient fluid is derived. In order to identify the components of the mixture, the sub-index $\alpha = 0, 1$ is used for fluid and solid phases, respectively.

2.2.1. *Constitutive relation for the interaction force between fluid and solid phases*

As the constituents of a fluid-solid mixture remain physically separated in the space, the interaction force between the constituents is identified as superficial forces acting on a singular surface that separates the phases (Bedford 1983; Drew 1983; Morland & Sellers 2001). In order to obtain the mathematical representation of the constitutive equation from the integral balance laws of momentum, we identify this singular surface as the border ∂V_1 of V_1 on which a tensor of interaction surface forces $\hat{T}_{01ij}$ acts. Considering this, the integral balance laws of momentum for the case of solid particles in a gravitational field are expressed as

$$\int_V \left\{ \frac{\partial \rho_1 u_{1i}}{\partial t} + \frac{\partial(\rho_1 u_{1j} u_{1i})}{\partial x_j} \right\} dV = \int_V \left\{ \rho_1 g_i + \frac{\partial T_{1ij}}{\partial x_j} \right\} dV + \int_{\partial V_1} \hat{T}_{01ij} n_j dS. \quad (2.3)$$

Applying the divergence theorem on the last term of (2.3), and since $dV_1 = c_1 dV$, then

$$\int_{\partial V_1} \hat{T}_{01ij} n_j dS = \int_{V_1} \frac{\partial \hat{T}_{01ij}}{\partial x_j} dV_1 = \int_V c_1 \frac{\partial \hat{T}_{01ij}}{\partial x_j} dV. \quad (2.4)$$

Defining $\hat{T}_{01ij}$ as the sum of a compression part $-\hat{p}_1 \delta_{ij}$, and a shear stress part $\hat{\tau}_{1ij}$, so

$$\hat{T}_{01ij} = -\hat{p}_{01} \delta_{ij} + \hat{\tau}_{01ij}, \quad (2.5)$$

where δ_{ij} denotes the delta Kronecker function, (2.3) is then written as

$$\frac{\partial \rho_1 u_{1i}}{\partial t} + \frac{\partial (\rho_1 u_{1j} u_{1i})}{\partial x_j} = \rho_1 g_i + \frac{\partial T_{1ij}}{\partial x_j} - c_1 \frac{\partial \hat{p}_{01}}{\partial x_i} + c_1 \frac{\partial \hat{\tau}_{01ij}}{\partial x_j}. \tag{2.6}$$

Hence, the interaction force between the fluid and the solids in the momentum equations (2.2) is identified as

$$\hat{m}_{1i} = -\hat{m}_{0i} = -c_1 \frac{\partial \hat{p}_{01}}{\partial x_i} + c_1 \frac{\partial \hat{\tau}_{01ij}}{\partial x_j}. \tag{2.7}$$

The normal stress component in (2.7), $\hat{p}_{01}$, arises from the saturation constraint; that is, $c_1 + c_0 = 1$, and it specifies how one phase transmits forces to another keeping the contact between the phases (Passman *et al.* 1984). Although this surface pressure was identified in early studies on two-phase flows (Bedford 1983), so far no agreement exists on the specific form of this part of the constitutive equation (Joseph & Lundgren 1990). Most works have considered an equal pressure for all phases and then for the interface pressure (e.g. Drew 1983; Morland 1992), but later investigations have shown that this assumption is not physically possible (e.g. Jackson 2000; Morland & Sellers 2001). For instance, equal pressure assumption forces to define the partial pressure of each phase as $p_\alpha = c_\alpha p$, where $p = p_1 + p_0$ is the pressure of the mixture. Under these circumstances, unphysical forces arise in the fluid phase given by volume concentration gradients, particularly under rest conditions, and an extra term, $p \partial_{x_i} c_0$, has to be included in order to obtain the correct force balance. We will analyse two simple cases in order to postulate that the interface pressure is the pressure of the fluid phase, and the correct mathematical representation for this interaction is presented in (2.7).

Let us consider first the static situation of a reservoir filled by solid particles with an interstitial fluid. The reduced weight of the solid particles is sustained by direct contacts among particles, identified here as the solid pressure p_1, and at places where no direct contact occurs the normal stress is the pressure of the surrounding fluid p_0. That is, the pressure of the fluid is sustained by both fluid and solid phases, while the reduced weight of the solids is sustained only by direct contacts among solid particles. Therefore, and in agreement with the Archimedes' principle, the interstitial fluid force balance is described between the equivalent weight of the fluid over the total mixture volume and the fluid pressure gradient, i.e. $\partial_{x_i} p_0 = \gamma_0 g_i$. Second, let us consider the dynamic case of solid particles falling down within a wide reservoir filled with a fluid, for instance water. We conducted laboratory tests by measuring the weight of such reservoir on a weigh scale and these revealed that while the particle were falling down, without touching the walls of the reservoir, the scale recorded the equivalent weight of water occupying the total volume of mixture, i.e. $\gamma_0(V_0 + V_1)g$, and only once the

particles impacted the bottom of the reservoir the balance recorded the total weight of the fluid-particles system, i.e. $(\gamma_0 V_0 + \gamma_1 V_1)g$. This second experiment shows the same fact described for the static case, that is, the reduced weight of the solid particles is not transmitted through the ambient fluid, so that different measurements will be recorded in the weigh scale depending on whether the particles are falling down or are resting on the bottom. These two simple analyses allow us to postulate that the interface pressure in (2.7) is the pressure of the fluid phase, p_0, i.e. $\hat{p}_{01} = p_0$. Thus, the normal interaction force is $-c_1 \partial_{x_i} p_0$, which can be identified as a buoyancy force, that is, it is the surface pressure exerted across the surface of the solids because of the surrounding fluid.

The last term of (2.7) arises from the stresses induced by the fluid when it passes through the interstices between the particles (e.g. Anderson & Jackson 1967). These stresses are well identified considering the fluidisation of a bed of particles at rest, in which a uniform upward fluid flow generates a drag force that counteracts the gravitational force (Sundaresan 2003). Although, as in the case of one solid particle immersed in a fluid, other effects arise because of the fluid-solid interactions, such as lift force, virtual mass effects and Basset force (Drew 1983), we consider only the total drag force, which can be written as (e.g. Di Felice 1995; Jackson 2000)

$$c_1 \frac{\partial \hat{\tau}_{01ij}}{\partial x_j} = (1 - \delta_{ij}) K_1 (u_{0i} - u_{1i}), \tag{2.8}$$

where K_1 is a well constrained phenomenological drag function (see Di Felice (1995) and references therein). Thus, (2.7) has the final frame indifferent form:

$$\hat{m}_{1i} = -\hat{m}_{0i} = -c_1 \frac{\partial p_0}{\partial x_i} + K_1 (u_{0i} - u_{1i}). \tag{2.9}$$

The drag function, K_1, is usually obtained through a generalisation of the drag force for a single particle by introducing a voidage function, $f_1(c_0)$, such as (Di Felice 1995)

$$K_1 = \frac{3}{4} C_{D1} \frac{\gamma_0}{d_1} |\boldsymbol{u}_0 - \boldsymbol{u}_1| c_1 f_1(c_0), \tag{2.10}$$

where d_1 is the diameter of the solid particles and C_{D1} is the drag coefficient given by Dallavalle (1948) as

$$C_{D1} = \left(0.63 + \frac{4.8}{\sqrt{Re_{d1}}} \right)^2, \tag{2.11}$$

where Re_{d1} is a modified particle Reynolds number, defined as $Re_{d1} = \rho_0 d_1 |\boldsymbol{u}_0 - \boldsymbol{u}_1|/\mu_0 = c_0 d_1 |\boldsymbol{u}_0 - \boldsymbol{u}_1|/\nu_0$, where μ_0 and ν_0 are the dynamic and kinematic viscosity of the fluid phase, respectively. The most common form for the voidage function is $f_1(c_0) = c_0^{2-\zeta_1}$, with ζ_1 a coefficient with values ranging from 3.6 to 3.7 for the viscous

and inertial flow regimes, respectively (Di Felice 1994). We use the coefficient proposed by Di Felice (1994) that fits empirically the two regimes as

$$\zeta_1 = 3.7 - 0.65 \exp\left[-\frac{(1.5 - \log(Re_{d1}))^2}{2}\right]. \tag{2.12}$$

2.2.2. *Stress tensor of the fluid phase*

Assuming that the state variables of the governing equation are mean quantities obtained by a Reynolds (1895) average of the equations, and using the eddy viscosity concept proposed by Boussinesq (1877) as a model for turbulent fluctuations, the stress tensor for the fluid phase can be written as (Rodi 1983)

$$T_{0ij} = -p_0 \delta_{ij} + (\mu_0 + \mu_T)\left(\frac{\partial u_{0i}}{\partial x_j} + \frac{\partial u_{0j}}{\partial x_i}\right), \tag{2.13}$$

where μ_T is the turbulent or eddy viscosity because of the velocity fluctuations from the mean flow. This eddy viscosity for the case of fluid-particles flows is more complicated than that for the case of pure fluid flows, because the solid particles modify the structure and intensity of the fluid turbulence, thus altering the transport rate of momentum (Elghobashi & Truesdell 1993). For instance, any slip between phases generates boundary layers around individual particles.

Although there are no general turbulent closures for the fluid phase in the case of two-phase flows, this issue is currently solved by including a source term in the kinetic energy equation of the fluid phase, which represents the irreversible work on the fluid associated with the drag force on the particles (Crowe *et al.* 1996). Following Crowe (2000), we propose a standard turbulence energy-dissipation model for the turbulence of the fluid phase ($k - \epsilon$ model, Rodi 1983), which includes the work done by the drag force as a production term in both k- and ϵ-equations. Then, the set of $k - \epsilon$ equations is written as

$$\mu_T = \rho_0 c_\mu \frac{k^2}{\epsilon}, \tag{2.14}$$

$$\frac{\partial(\rho_0 k)}{\partial t} + \frac{\partial(\rho_0 u_{0i} k)}{\partial x_i} = \frac{\partial}{\partial x_i}\left(\frac{\mu_T}{\sigma_\beta}\frac{\partial k}{\partial x_i}\right) + \mu_T\left(\frac{\partial u_{0i}}{\partial x_j} + \frac{\partial u_{0j}}{\partial x_i}\right)\frac{\partial u_{0i}}{\partial x_j}$$
$$+ K_1|\boldsymbol{u}_0 - \boldsymbol{u}_1|^2 - \rho_0\epsilon, \tag{2.15}$$

$$\frac{\partial(\rho_0 \epsilon)}{\partial t} + \frac{\partial(\rho_0 u_{0i}\epsilon)}{\partial x_i} = c_{1\epsilon}\frac{\epsilon}{k}\left[\mu_T\left(\frac{\partial u_{0i}}{\partial x_j} + \frac{\partial u_{0j}}{\partial x_i}\right)\frac{\partial u_{0i}}{\partial x_j} + K_1|\boldsymbol{u}_0 - \boldsymbol{u}_1|^2\right]$$
$$+ \frac{\partial}{\partial x_i}\left(\frac{\mu_T}{\sigma_\epsilon}\frac{\partial \epsilon}{\partial x_i}\right) - c_{2\epsilon}\rho_0\frac{\epsilon^2}{k}, \tag{2.16}$$

where k is the kinetic energy of the fluid turbulent motion, and ϵ is the dissipation rate of k. The values of the constants in (2.14)-(2.16) are taken equal to the standard values for a pure fluid: c_μ=0.09, $c_{1\epsilon}$=1.44, $c_{2\epsilon}$=1.92, σ_β=1.00, and σ_ϵ=1.30 (Rodi 1983; Pope 2000).

2.2.3. *Stress tensor of the solid phase*

The stress tensor of the solid particles represents the forces transmitted by direct inter-particle contacts. These forces are well-known for two opposite regimes of the granular flow. On the one hand, the dilute and rapid granular flow regime in which the particles interact by binary collisions (Campbell 1990; Goldhirsch 2003), and on the other hand, the dense quasi-static regime in which the onset of the flow is determined by the Mohr-Coulomb condition (Hutter *et al.* 2005). However, the constitutive equation for the intermediate regime in which both collisional and frictional interactions might be important is not well-known (Forterre & Pouliquen 2008). In order to take into account these three regimes, we will follow the assumption of Savage (1983) and Johnson & Jackson (1987), who proposed that the stress tensor of the solid particles is represented by the linear sum of a rate-independent quasi-static part, T_{1ij}^s, and a rate-dependent collisional part, T_{1ij}^c, such as

$$T_{1ij} = T_{1ij}^s + T_{1ij}^c. \tag{2.17}$$

The rate-independent quasi-static part, T_{1ij}^s, can be decomposed as

$$T_{1ij}^s = -p_1 \delta_{ij} + \tau_{1ij}, \tag{2.18}$$

where p_1 is the solid pressure (assumed isotropic) and τ_{1ij} is the solid shear stress tensor. We define the solid pressure as the reaction force that arises in response to the constraint of incompressibility when the solid particles are packed, which in the static case can be interpreted as the fraction of the weight of the solids that is sustained by direct contacts among solid particles or at boundaries. Accordingly, the solid pressure can be written as

$$p_1(c_1) = \begin{cases} p_1 & c_1 \geqslant c, \\ 0 & c_1 < c, \end{cases} \tag{2.19}$$

where c is the loose packing concentration defined as the lowest stable packing of particles. Mathematically, the inclusion of the closure (2.19) means that one of the two variables, c_1 or p_1, will be constant depending on whether the flow is packed or not. When the granular flow is packed, i.e. when it is incompressible, the solid density $\rho_1 = c_1 \gamma_1$ is constant; in contrast, when the granular flow is unpacked, i.e. when it is compressible, p_1 is equal to zero. In fact, this model ensures that once the granular flow is unpacked, the maximum concentration that it can acquire is the loose packing value.

The quasi-static solid shear stress tensor, τ_{1ij}, is represented by the Mohr-Coulomb condition, which states that the compressible and shear stresses acting in a particular plane over a particular point are related by (e.g. Goodman & Cowin 1971)

$$|\tau_{1ij}| = (1 - \delta_{ij})|p_1|\tan\varphi, \tag{2.20}$$

where φ is the internal friction angle. Note that because of the closure of (2.19), the solid shear stress also vanishes when the flow is unpacked.

The rate-dependent collisional part, T_1^c, on the other hand, arises in a rapid sheared flow in which each particle has a random fluctuation of the velocity respect to the mean flow. As this random motion arises from particles collisions, the granular flow is represented in a similar way as the thermal motion of molecules in the kinetic theory of gases, considering additionally the energy loss because of inelastic collisions (Campbell 1990; Goldhirsch 2003). We use the kinetic theory proposed by Jenkins & Savage (1983), in which the collisional stress tensor can be written as

$$T_{1ij}^c = -p_c\delta_{ij} + 2\mu_c\dot{\gamma}_{1ij}, \tag{2.21}$$

where $\dot{\gamma}_{1ij} = (\partial_{x_j}u_{1i} + \partial_{x_i}u_{1j})$ is the shear rate tensor, $p_c = \gamma_1 f_a(c_1, e)T$ is the collisional pressure, $\mu_c = \gamma_1 d_1 f_b(c_1, e)\sqrt{T}$ is the collisional viscosity, with $T = \langle u_{1i}'^2 \rangle/3$ the granular temperature, where u_{1i}' is the instantaneous deviation from the mean velocity, and $\langle\rangle$ represents an ensemble average. In this model, the parameterizations $f_a(c_1, e)$ and $f_b(c_1, e)$ are equal to

$$f_a(c_1, e) = 2c_1^2(1 + e)g(c_1), \quad f_b(c_1, e) = \frac{2}{5\sqrt{\pi}}c_1^2(2 + \delta)(1 + e)g(c_1), \tag{2.22}$$

where e is the coefficient of restitution, δ is a parameter equal to one as Lun *et al.* (1984) suggested, and $g(c_1)$ is the radial distribution function. We use the function proposed by Lun *et al.* (1984) that is implicit in the work of Bagnold (1954)

$$g(c_1) = \left[1 - \left(\frac{c_1}{c_M}\right)^{1/3}\right]^{-1}, \tag{2.23}$$

where c_M is the dense packing concentration equal to 0.64 for spheres (Lun *et al.* 1984). Finally, we relate this model with our representation through the relation between the shear rate and the granular temperature $S = d_1\dot{\gamma}_1 T^{-1/2}$, for which $S \approx 1$ in most of the range of the solid concentration (Campbell 2006), so that we consider

$$T = (d_1\dot{\gamma}_1)^2, \tag{2.24}$$

where $\dot{\gamma}_1 = \sqrt{1/2|\dot{\gamma}_{1ii}^2 - \dot{\gamma}_{1ij}\dot{\gamma}_{1ji}|}$ is the root of the second invariant of the shear rate tensor.

The final system of two-phase equations is represented by:

$$\frac{\partial \rho_\alpha}{\partial t} + \frac{\partial(\rho_\alpha u_{\alpha i})}{\partial x_i} = 0, \quad \alpha = 0, 1, \tag{2.25}$$

$$\frac{\partial \rho_0 u_{0i}}{\partial t} + \frac{\partial(\rho_0 u_{0j} u_{0i})}{\partial x_j} = \rho_0 g_i - c_0 \frac{\partial p_0}{\partial x_i} + \frac{\partial}{\partial x_j}\left[(\mu_0 + \mu_T)\left(\frac{\partial u_{0i}}{\partial x_j} + \frac{\partial u_{0j}}{\partial x_i}\right)\right]$$
$$- K_1(u_{0i} - u_{1i}), \tag{2.26}$$

$$\frac{\partial \rho_1 u_{1i}}{\partial t} + \frac{\partial(\rho_1 u_{1j} u_{1i})}{\partial x_j} = \rho_1 g_i - \frac{\partial p_1}{\partial x_i} + s_{ij}\frac{\partial p_1}{\partial x_j}\tan\varphi + \frac{\partial}{\partial x_j}\left[\mu_c\left(\frac{\partial u_{1i}}{\partial x_j} + \frac{\partial u_{1j}}{\partial x_i}\right)\right]$$
$$- \frac{\partial p_c}{\partial x_i} - c_1\frac{\partial p_0}{\partial x_i} + K_1(u_{0i} - u_{1i}), \tag{2.27}$$

where $s_{ij} \equiv sgn(\partial_{x_j} u_{1i})$. This system of equations is closed with the saturation constraint $c_1 + c_0 = 1$, and (2.10)-(2.12), (2.14)-(2.16), (2.19), (2.22)-(2.24).

2.3. Dense heterogeneous granular flows

In this section, we extend the two-phase approach proposed in the previous section to the case of dense heterogeneous mixtures of solid particles, by including in the momentum equations a constitutive relation that describes the interaction mechanisms between the solid constituents in a dense regime. In order to identify the components of the mixture, the sub-index $\alpha = 0$ and $\alpha = 1, 2, ..., N$ are used for fluid and solids constituents, respectively.

2.3.1. *Stress tensor of the solid constituents in a dense regime*

According to (2.17) the stress tensor of the solid constituents in a dense regime is represented by the rate-independent quasi-static part, which was decomposed as $T_{\alpha ij} = -p_\alpha \delta_{ij} + \tau_{\alpha ij}$, $\alpha = 1, 2, ..., N$, where p_α is the pressure of the constituent α (assumed isotropic), and $\tau_{\alpha ij}$ is the shear stress tensor of the constituent α. The solid pressure, p_α, was defined as the reaction force that arises in response to the constraint of incompressibility when the solid particles are packed, which in the static case can be interpreted as the fraction of the weight of the solids that is sustained by direct contacts among solid particles or at boundaries. Here we extend that definition and interpret the solid pressure of the constituent α as the reaction force related to the constraint

of incompressibility when the particles of the constituent α are packed, which can be mathematically represented by

$$p_\alpha = \begin{cases} p_\alpha & c_\alpha \geqslant c_\alpha^*, \\ 0 & c_\alpha < c_\alpha^*, \end{cases} \quad \alpha = 1, 2, ..., N, \tag{2.28}$$

where c_α^* is the loose packing concentration of the solid constituent α, which depends on the relative particle diameter and the local concentration of each solid constituent of the mixture, as discussed in § 2.4.

Furthermore, the shear stress tensor of the constituent α is represented by the Mohr-Coulomb condition:

$$|\tau_{\alpha ij}| = (1 - \delta_{ij})|p_\alpha| \tan \varphi_\alpha, \, \alpha = 1, 2, ..., N, \tag{2.29}$$

where φ_α is the internal friction angle of the solid constituent α. Note that because of the closure of (2.28), the solid shear stress also vanishes when the constituent α is unpacked, which is an approximation as stresses may arise due to particles collisions (Campbell 1990; Goldhirsch 2003). These collisional stresses, however, are not considered here because we focus on dense granular flows for which long-lived contact stresses dominate the flow dynamics (Campbell 2006).

2.3.2. *Constitutive relation for the interaction force between solid constituents in a dense regime*

For obtaining the constitutive relation that represents the interaction force between the solid components, $\hat{m}_{\beta\alpha i} = -\hat{m}_{\alpha\beta i}$, we follow the second guiding principle proposed by Truesdell (1957) to describe the motion of a constituent. This principle states that we may, in imagination, isolate a constituent from the rest of the mixture as long as the effects of the other components are considered as forces acting upon it. In this context, let us do the abstraction of a volume V_α, containing only particles of the solid constituent α and surrounded by a mixture that contains all the other components (figure 2.1a). This abstraction allows us to interpret the actions of the other solid components on the constituent α as superficial forces acting on the surface ∂V_α of V_α, such as the action force of the component $\beta \neq \alpha = 1, ..., N$ on α can be represented by a tensor of superficial forces $\hat{T}_{\beta\alpha ij}$ acting on ∂V_α (note that the case $\beta = 0$ is analyzed in § 2.3.3). In this way, the action force of the constituent β on α is $\int_{\partial V_\alpha} \hat{T}_{\beta\alpha ij} n_j \, dS$, with n_j the outward normal vector, and in response there is an equivalent and opposite force acting on β, $- \int_{\partial V_\alpha} \hat{T}_{\beta\alpha ij} n_j \, dS$. Similarly, if we now consider the same abstraction for the constituent β (figure 2.1b), then the action force of the solid constituent $\alpha \neq \beta = 1, ..., N$ on β is $\int_{\partial V_\beta} \hat{T}_{\alpha\beta ij} n_j \, dS$, and in response there is an equivalent and opposite force acting on α, $- \int_{\partial V_\beta} \hat{T}_{\alpha\beta ij} n_j \, dS$. Thus, the reciprocal interaction force between the constituents
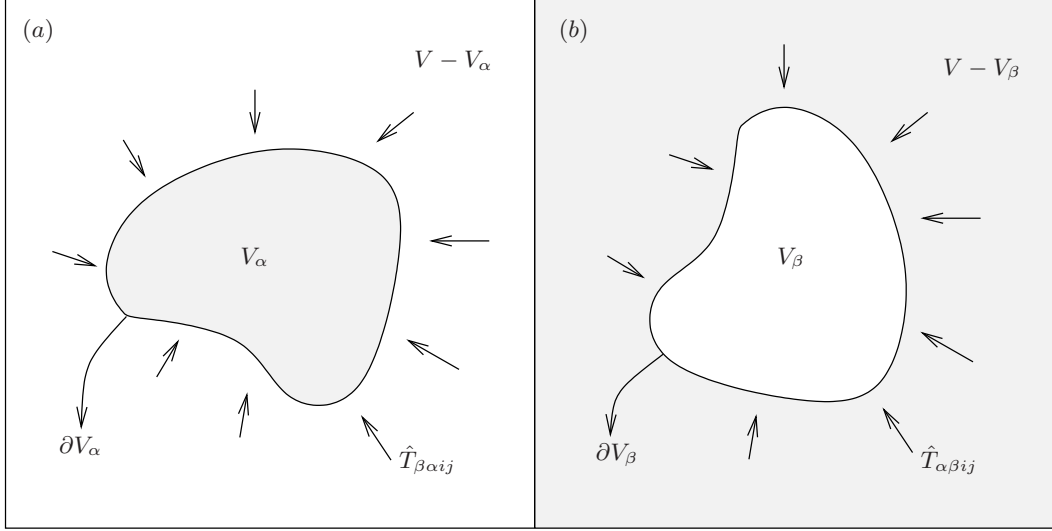
FIGURE 2.1. In imagination the solid constituents α and β are isolated from the rest of the mixture. (a) $\int_{\partial V_\alpha} \hat{T}_{\beta\alpha ij} n_j dS$ corresponds to the action force of the solid constituent β acting on the surface ∂V_α of V_α, and in response there is an equivalent and apposite force acting on β, $-\int_{\partial V_\alpha} \hat{T}_{\beta\alpha ij} n_j dS$. (b) In the same way, $\int_{\partial V_\beta} \hat{T}_{\alpha\beta ij} n_j dS$ corresponds to the action force of the solid constituent α acting on the surface ∂V_β of V_β, and in response there is an equivalent and apposite force acting on α, $-\int_{\partial V_\beta} \hat{T}_{\alpha\beta ij} n_j dS$. Thus, the mutual actions between constituents are represented by $\int_V \hat{m}_{\beta\alpha i} dV = -\int_V \hat{m}_{\alpha\beta i} dV = \int_{\partial V_\alpha} \hat{T}_{\beta\alpha ij} n_j dS - \int_{\partial V_\beta} \hat{T}_{\alpha\beta ij} n_j dS$.

α and β has two components, one representing the action force of the constituent β on the constituent α that is applied on the border ∂V_α, and another representing the reaction force of the constituent β on the constituent α that is applied on the border ∂V_β, such as the reciprocal force is represented by

$$\int_V \hat{m}_{\beta\alpha i} \, dV = -\int_V \hat{m}_{\alpha\beta i} \, dV = \int_{\partial V_\alpha} \hat{T}_{\beta\alpha ij} n_j \, dS - \int_{\partial V_\beta} \hat{T}_{\alpha\beta ij} n_j \, dS. \tag{2.30}$$

Applying the divergence theorem and since $dV_\alpha = c_\alpha \, dV$, so that

$$\int_{\partial V_\alpha} \hat{T}_{\beta\alpha ij} n_j \, dS = \int_{V_\alpha} \frac{\partial \hat{T}_{\beta\alpha ij}}{\partial x_j} \, dV_\alpha = \int_V c_\alpha \frac{\partial \hat{T}_{\beta\alpha ij}}{\partial x_j} \, dV, \tag{2.31}$$

(2.30) is then written as

$$\hat{m}_{\beta\alpha i} = -\hat{m}_{\alpha\beta i} = c_\alpha \frac{\partial \hat{T}_{\beta\alpha ij}}{\partial x_j} - c_\beta \frac{\partial \hat{T}_{\alpha\beta ij}}{\partial x_j}. \tag{2.32}$$

Defining $\hat{T}_{\beta\alpha ij}$ as the sum of a compression part $-\hat{p}_{\beta\alpha}$, and a shear stress part $\hat{\tau}_{\beta\alpha ij}$, so that $\hat{T}_{\beta\alpha ij} = -\hat{p}_{\beta\alpha}\delta_{ij} + \hat{\tau}_{\beta\alpha ij}$, the first component of (2.32) that represents the action

force of β on α, is then written as

$$c_\alpha \frac{\partial \hat{T}_{\beta\alpha ij}}{\partial x_j} = -c_\alpha \frac{\partial \hat{p}_{\beta\alpha}}{\partial x_i} + c_\alpha \frac{\partial \hat{\tau}_{\beta\alpha ij}}{\partial x_j}. \tag{2.33}$$

The normal interaction term of (2.33), $-c_\alpha \partial \hat{p}_{\beta\alpha}/\partial x_i$, can be interpreted as a buoyancy force, as it represents the normal force exerted by the constituent β on the surface of the constituent α, so that $\hat{p}_{\beta\alpha}$ is the pressure of the constituent β, i.e. p_β. The shear interaction term of (2.33), $c_\alpha \partial \hat{\tau}_{\beta\alpha ij}/\partial x_j$, on the other hand, represents the tangential force exerted by the constituent β on the surface of the constituent α, so that by analogy to the homogeneous dense flow regime, the shear stress component, $\hat{\tau}_{\beta\alpha ij}$, can be represented by the Mohr-Coulomb condition:

$$|\hat{\tau}_{\beta\alpha ij}| = (1 - \delta_{ij})|\hat{p}_{\beta\alpha}| \tan \varphi_{\beta\alpha} = (1 - \delta_{ij})|p_\beta| \tan \varphi_{\beta\alpha}, \tag{2.34}$$

where $\varphi_{\beta\alpha}$ represents the internal friction angle between the constituents β and α. Therefore, the final action force of the constituent β on α in a dense regime is represented by

$$c_\alpha \frac{\partial \hat{T}_{\beta\alpha ij}}{\partial x_j} = -c_\alpha \frac{\partial p_\beta}{\partial x_i} - s_{\beta\alpha ij} c_\alpha \tan \varphi_{\beta\alpha} \frac{\partial p_\beta}{\partial x_j}, \tag{2.35}$$

where $s_{\beta\alpha ij} \equiv \mathrm{sgn}\,(\partial(u_{\beta i} - u_{\alpha i})/\partial x_j)$. In the same way, the second component of (2.32), which represents the reaction force of the constituent β on α due to the action force of α on β, is represented by

$$- c_\beta \frac{\partial \hat{T}_{\alpha\beta ij}}{\partial x_j} = c_\beta \frac{\partial p_\alpha}{\partial x_i} + s_{\alpha\beta ij} c_\beta \tan \varphi_{\alpha\beta} \frac{\partial p_\alpha}{\partial x_j}, \tag{2.36}$$

such as the final reciprocal interaction force is

$$\hat{m}_{\beta\alpha i} = -\hat{m}_{\alpha\beta i} = -c_\alpha \frac{\partial p_\beta}{\partial x_i} - s_{\beta\alpha ij} c_\alpha \tan \varphi_{\beta\alpha} \frac{\partial p_\beta}{\partial x_j} + c_\beta \frac{\partial p_\alpha}{\partial x_i} + s_{\alpha\beta ij} c_\beta \tan \varphi_{\alpha\beta} \frac{\partial p_\alpha}{\partial x_j}, \tag{2.37}$$

and the total interaction force acting on the solid constituent α due to the other components of the mixture is then

$$\hat{m}_{\alpha i} = \sum_{\beta \neq \alpha = 0}^{N} \hat{m}_{\beta\alpha i} = \hat{m}_{0\alpha i} + \sum_{\beta \neq \alpha = 1}^{N} \left\{ -c_\alpha \frac{\partial p_\beta}{\partial x_i} + c_\beta \frac{\partial p_\alpha}{\partial x_i} - s_{\beta\alpha ij} \tan \varphi_{\beta\alpha} \left(c_\alpha \frac{\partial p_\beta}{\partial x_j} + c_\beta \frac{\partial p_\alpha}{\partial x_j} \right) \right\}, \tag{2.38}$$

where $\hat{m}_{0\alpha i}$ is the interaction force with the ambient fluid ($\beta = 0$), $s_{\beta\alpha ij} = -s_{\alpha\beta ij}$ and $\varphi_{\beta\alpha} = \varphi_{\alpha\beta}$.

2.3.3. *Constitutive relation for the interaction force between the fluid and the solids*

According to (2.9), the interaction force between the ambient fluid ($\alpha=0$) and each solid constituent can be written as

$$\hat{m}_{\beta 0i} = c_\beta \frac{\partial p_0}{\partial x_i} - K_\beta(u_{0i} - u_{\beta i}), \ \beta = 1, 2, ..., N, \tag{2.39}$$

As discussed, the first component of this interaction term, $c_\beta \partial p_0 / \partial x_i$, represents the reaction force of the solid constituent β in response to the buoyancy force exerted by the fluid; and the second component, $-K_\beta(u_{0i} - u_{\beta i})$, represents the reaction force of the solid constituent β in response to the drag force induced by the fluid when it passes through the interstices between the particles of the solid constituent β.

Thus, the total interaction force acting on the ambient fluid due to the solid constituents can then be written as

$$\hat{m}_{0i} = \sum_{\beta=1}^{N} \hat{m}_{\beta 0i} = (1 - c_0) \frac{\partial p_0}{\partial x_i} - \sum_{\beta=1}^{N} K_\beta(u_{0i} - u_{\beta i}). \tag{2.40}$$

From (2.10)-(2.12), the drag function, K_β, can be written as

$$K_\beta = \frac{3}{4} C_{D\beta} \frac{\gamma_0}{d_\beta} |\boldsymbol{u}_0 - \boldsymbol{u}_\beta| c_\beta f_\beta(c_0), \ \beta = 1, 2, ..., N, \tag{2.41}$$

where d_β is the diameter of the solid particles and $C_{D\beta}$ is the drag coefficient given by

$$C_{D\beta} = \left(0.63 + \frac{4.8}{\sqrt{Re_{d\beta}}}\right)^2, \ \beta = 1, 2, ..., N. \tag{2.42}$$

with $Re_{d\beta} = \rho_0 d_\beta |\boldsymbol{u}_0 - \boldsymbol{u}_\beta| / \mu_0$, $f_\beta(c_0) = c_0^{2-\zeta_\beta}$, and ζ_β given by

$$\zeta_\beta = 3.7 - 0.65 \exp\left[-\frac{(1.5 - \log(Re_{d\beta}))^2}{2}\right]. \tag{2.43}$$

2.3.4. *Stress tensor of the ambient fluid*

The stress tensor for the ambient fluid is given by (2.13), for which the turbulent or eddy viscosity due to the velocity fluctuations from the mean flow, μ_T, is obtained from the standard turbulence energy-dissipation model ($k - \epsilon$ model, Rodi 1983). In this case of several solid constituents, the $k - \epsilon$ model have to include the work done by the drag force of each solid constituent as a production term in both k- and ϵ-equations

(Crowe *et al.* 1996). Then, the set of $k - \epsilon$ equations are written as

$$\mu_T = \rho_0 c_\mu \frac{k^2}{\epsilon}, \tag{2.44}$$

$$\begin{aligned}
\frac{\partial(\rho_0 k)}{\partial t} + \frac{\partial(\rho_0 u_{0i} k)}{\partial x_i} &= \frac{\partial}{\partial x_i}\left(\frac{\mu_T}{\sigma_k}\frac{\partial k}{\partial x_i}\right) + \mu_T\left(\frac{\partial u_{0i}}{\partial x_j} + \frac{\partial u_{0j}}{\partial x_i}\right)\frac{\partial u_{0i}}{\partial x_j} \\
&\quad + \sum_{\beta=1}^{N} K_\beta |\boldsymbol{u}_0 - \boldsymbol{u}_\beta|^2 - \rho_0 \epsilon,
\end{aligned} \tag{2.45}$$

$$\begin{aligned}
\frac{\partial(\rho_0 \epsilon)}{\partial t} + \frac{\partial(\rho_0 u_{0i} \epsilon)}{\partial x_i} &= c_{1\epsilon}\frac{\epsilon}{k}\left[\mu_T\left(\frac{\partial u_{0i}}{\partial x_j} + \frac{\partial u_{0j}}{\partial x_i}\right)\frac{\partial u_{0i}}{\partial x_j} + \sum_{\beta=1}^{N} K_\beta |\boldsymbol{u}_0 - \boldsymbol{u}_\beta|^2\right] \\
&\quad + \frac{\partial}{\partial x_i}\left(\frac{\mu_T}{\sigma_\epsilon}\frac{\partial \epsilon}{\partial x_i}\right) - c_{2\epsilon}\rho_0\frac{\epsilon^2}{k},
\end{aligned} \tag{2.46}$$

The values of the constants in (2.44), (2.45) and (2.46) are taken equal to the standard values for a pure fluid: c_μ=0.09, $c_{1\epsilon}$=1.44, $c_{2\epsilon}$=1.92, σ_k=1.00, and σ_ϵ=1.30 (Rodi 1983; Pope 2000).

2.3.5. *Final form of the multi-species equations*

The final system of governing equations is represented by:

$$\frac{\partial \rho_\alpha}{\partial t} + \frac{\partial(\rho_\alpha u_{\alpha i})}{\partial x_i} = 0, \quad \alpha = 0, 1, ..., N, \tag{2.47}$$

$$\begin{aligned}
\frac{\partial \rho_0 u_{0i}}{\partial t} + \frac{\partial(\rho_0 u_{0j} u_{0i})}{\partial x_j} &= \rho_0 g_i - c_0\frac{\partial p_0}{\partial x_i} + \frac{\partial}{\partial x_j}\left[(\mu_0 + \mu_T)\left(\frac{\partial u_{0i}}{\partial x_j} + \frac{\partial u_{0j}}{\partial x_i}\right)\right] \\
&\quad - \sum_{\beta=1}^{N} K_\beta(u_{0i} - u_{\beta i}),
\end{aligned} \tag{2.48}$$

$$\begin{aligned}
\frac{\partial \rho_\alpha u_{\alpha i}}{\partial t} &+ \frac{\partial(\rho_\alpha u_{\alpha j} u_{\alpha i})}{\partial x_j} = \rho_\alpha g_i - \frac{\partial p_\alpha}{\partial x_i} + s_{\alpha ij}\frac{\partial p_\alpha}{\partial x_j}\tan\varphi_\alpha - c_\alpha\frac{\partial p_0}{\partial x_i} + K_\alpha(u_{0i} - u_{\alpha i}) \\
&+ \sum_{\beta\neq\alpha=1}^{N}\left\{-c_\alpha\frac{\partial p_\beta}{\partial x_i} + c_\beta\frac{\partial p_\alpha}{\partial x_i} - s_{\beta\alpha ij}\tan\varphi_{\beta\alpha}\left(c_\alpha\frac{\partial p_\beta}{\partial x_j} + c_\beta\frac{\partial p_\alpha}{\partial x_j}\right)\right\}, \quad \alpha = 1, 2, ..., N,
\end{aligned} \tag{2.49}$$

where $s_{\alpha ij} \equiv sgn(\partial_{x_j} u_{\alpha i})$. This system of equations is closed with the saturation constraint $\sum_{\alpha=0}^{N} c_\alpha = 1$, and (2.28), (2.41)-(2.43), (2.44)-(2.46).

2.4. Binary mixtures of small and large spherical grains

In this section, we analyse the particular case of binary mixtures of small and large spherical particles. By denoting $\alpha = 1, 2$ to small and large grains, respectively, three solid packing concentrations are used in the solid pressure closure (2.28) to determine whether the solid pressure of each constituent is zero or not: the loose packing value of the mixture, c^*, and the loose packing values of small and large particles, c_1^* and c_2^*, respectively. Here, we discuss these values and the criterion for calculating the solid pressure for each solid constituent.

2.4.1. *Packing concentration of binary mixtures of spherical grains*

Binary mixtures of small and large spherical grains can pack to higher concentrations than assemblages of monosized grains, and the improvement on the packing concentration depends on the size ratio, d_1/d_2, and on the fractional solid concentration of each constituent, $X_\alpha = c_\alpha/(c_1 + c_2)$, α=1,2 (German 1989, pp. 135 - 163). Several models account for the influence of these parameters on the packing of mixtures (German 1989, pp. 135 - 163), and we chose the empirical formula of Fedors & Landel (1979) that for bimodal spheres of the same composition and packing concentration can be written as

$$c^* \left(d_1/d_2, X_2\right) = \begin{cases} \left(1 - \sqrt{d_1/d_2}\right) c(1-c)(2-c)X_2 + c & X_2 \leqslant 1/(2-c), \\ \left(1 - \sqrt{d_1/d_2}\right) c(2-c)(1-X_2) + c & X_2 > 1/(2-c), \end{cases} \tag{2.50}$$

where c is the loose packing concentration of monosized particles that is equal to 0.6 for spheres (e.g. Rutgers 1962). An example of the dependence of the packing concentration with the relative concentration of the small grains, $X_1 = 1 - X_2$, is shown in figure 2.2, in which is observed that the optimal packing is found for % of small grains close to 28%, case for which the small spheres fill all the voids in the large sphere packing (German 1989, pp. 140). Furthermore, the loose packing concentration of each solid constituent can be written as

$$c_\alpha^* = c^* - c_\beta, \;\; \alpha \neq \beta = 1, 2. \tag{2.51}$$

2.4.2. *Criterion for the calculation of the solid pressure*

The inclusion of the loose packing limits (2.51) in the solid pressure closure (2.28) means that for mixture concentrations less than c^* both small and large particles loose their contacts and fall down, if there are no other forces that can support their weight. However, it is well known that below a critical value of the mixture concentration, only the small particles fall down while the large particles remain packed. This is because the small particles have a greater probability than the large ones of finding a hole in which they can fall into (Savage & Lun 1988), so that the packing limit of small and
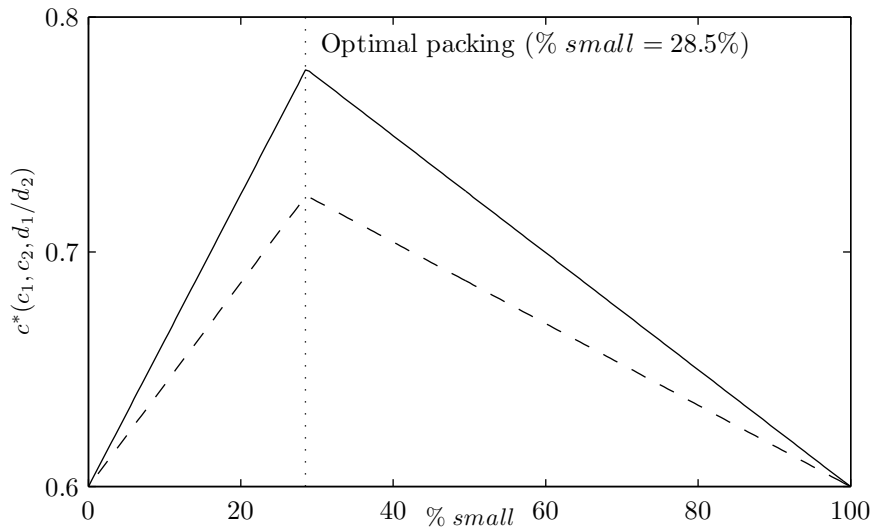
FIGURE 2.2. Calculated loose packing concentration of binary mixtures of small and large grains using (2.51) and c=0.6, d_1/d_2=0.07 (solid line) and d_1/d_2=0.22 (dashed line).

large particles should be different. We make two assumptions: first, ηc^* ($\eta \leqslant 1$) is the limit under which (i.e. $c_1 + c_2 < \eta c$) both large and small particles fall down, where $\eta \leqslant 1$ is an empirical parameter; second, c^* is the limit under which (i.e. $c_1 + c_2 < c^*$) the small particles percolate downward while the large particle remain packed. In this way, the loose packing concentration used in the pressure closure (2.28) for small and large particles is represented by

$$c_1^* = c^* - c_2, \ \ c_2^* = \eta c^* - c_1. \tag{2.52}$$

The empirical function η has to preserve the physical limit of $\eta = 1$ when $c_1 = 0$ or $c_2 = 0$ or $d_1 = d_2$, and it should increase with d_1/d_2, so that we propose the following expression:

$$\eta(c_1, c_2, d_1/d_2) = exp\left(-\sigma c_1 c_2 [1 - d_1/d_2]\right), \tag{2.53}$$

with $\sigma > 0$ an empirical constant order one that is discussed in §5.2.

An additional condition that should be considered is the sifting of small grains when $d_1/d_2 < (2/\sqrt{3} - 1) \approx 0.15$, which corresponds to the Apollonian ratio in which a small particle exactly fit inside a hole between three tangent spheres in the packing of the larger particles (Ippolito *et al.* 2000). This means that when $d_1/d_2 < 0.15$ and the large particles are in point contact with one another, i.e. $c_2 \geqslant c$, percolation of small particles occurs spontaneously as long as the interstitial voids between the large particles are not filled, i.e. $c_1 < (1 - \sqrt{d_1/d_2})c(1 - c)$ (German 1989, pp. 135 - 163).

Considering these restrictions, the final conditions for the calculation of the solid

pressure for small and large particles are given by

$$
p_1(c_1, c_2, c^*, d_1/d_2) = \begin{cases} p_1 & \begin{cases} d_1/d_2 \geqslant 0.15 \quad \& \quad c_1 \geqslant (c^* - c_2) \\ & \qquad\quad c_2 \geqslant c \, \& \, c_1 \geqslant (1 - \sqrt{d_1/d_2})c(1-c) \\ d_1/d_2 < 0.15 \quad \& \quad or \\ & \qquad\quad c_2 < c \, \& \, c_1 \geqslant (c^* - c_2) \\ 0 & \qquad\qquad otherwise \end{cases} \end{cases}
$$

$$(2.54)$$

$$
p_2(c_1, c_2, c^*, d_1/d_2) = \begin{cases} p_2 & \begin{cases} d_1/d_2 \geqslant 0.15 \quad \& \quad c_2 \geqslant (\eta c^* - c_1) \\ & \qquad\qquad c_2 \geqslant c \\ d_1/d_2 < 0.15 \quad \& \quad or \\ & \qquad\quad c_2 < c \, \& \, c_2 \geqslant (\eta c^* - c_1) \\ 0 & \qquad\qquad otherwise \end{cases} \end{cases}
$$

$$(2.55)$$

Chapter 3

Methods

3.1. Experimental procedure

Experiments were conducted in a 1.5 m-long perspex rectangular channel, 0.5 m-deep and 0.1 m-wide, by suddenly opening a vertical gate that initially hold a granular column in air or water (the water depth was 0.45 m). The initial column aspect ratio h_o/x_o was in the range [1,16], with h_o and x_o the initial height and length, respectively. The experimental facility is shown in figure 3.1, in which is shown the initial experimental set up (figure 3.1 a), and the sketch of the final deposits in air (figure 3.1 b) and in water (figure 3.1 c).

We first did experiments with monosized glass beads of three particle sizes $d_1 = $ 0.2, 0.7, 3.0 mm, with a total of six sets of experiments listed in table 3.1. Then, we combined the grains in order to obtain binary mixtures of small and large glass beads with mixtures of 0.2 and 3.0 mm, and 0.7 and 3.0 mm, with a total of four sets of experiments listed in table 3.2.

The physical properties presented in tables 3.1 and 3.2 correspond to the typical mean values of the materials used at 20 ^{o}C, and we measured the loose packing concentration of the monosized particles ($c = 0.6 \pm 0.2$) as well as the internal friction angle ($\varphi = 26 \pm 3$ deg). The loose packing volume concentration was estimated by measuring the volume of water displaced when a known volume of packed particles is immersed in water. The internal angle of friction was assumed to be equal to the angle of repose, which was estimated by pouring the particles on a rough horizontal plane from a fixed source. The angle below which the heap stays unchanged at rest and above which surface motion down slope starts was considered as the internal friction angle. This angle is in the range measured in other experimental studies with subspherical glass beads (e.g. Balmforth & Kerswell 2005; Lajeunesse *et al.* 2005).

Each set of experiments of binary mixtures was carried out by varying the proportion of small and large glass beads. In case of mixtures with $d_1/d_2 \geqslant 0.15$ (sets B1 and B2 in table 3.2) we used homogeneous mixtures with four initial relative solid concentrations of small particles: $\% \; small \equiv 100(h_o x_o)^{-1} \int_0^{h_o} \int_0^{x_o} (c_1/[c_1 + c_2])_{t=0} \, dx dy$ equal to 0, 25, 50 and 100%. In contrast, for mixtures with $d_1/d_2 <0.15$ (sets A1 and A2 in table 3.2), for which percolation of small particles occurs spontaneously when the interstitial
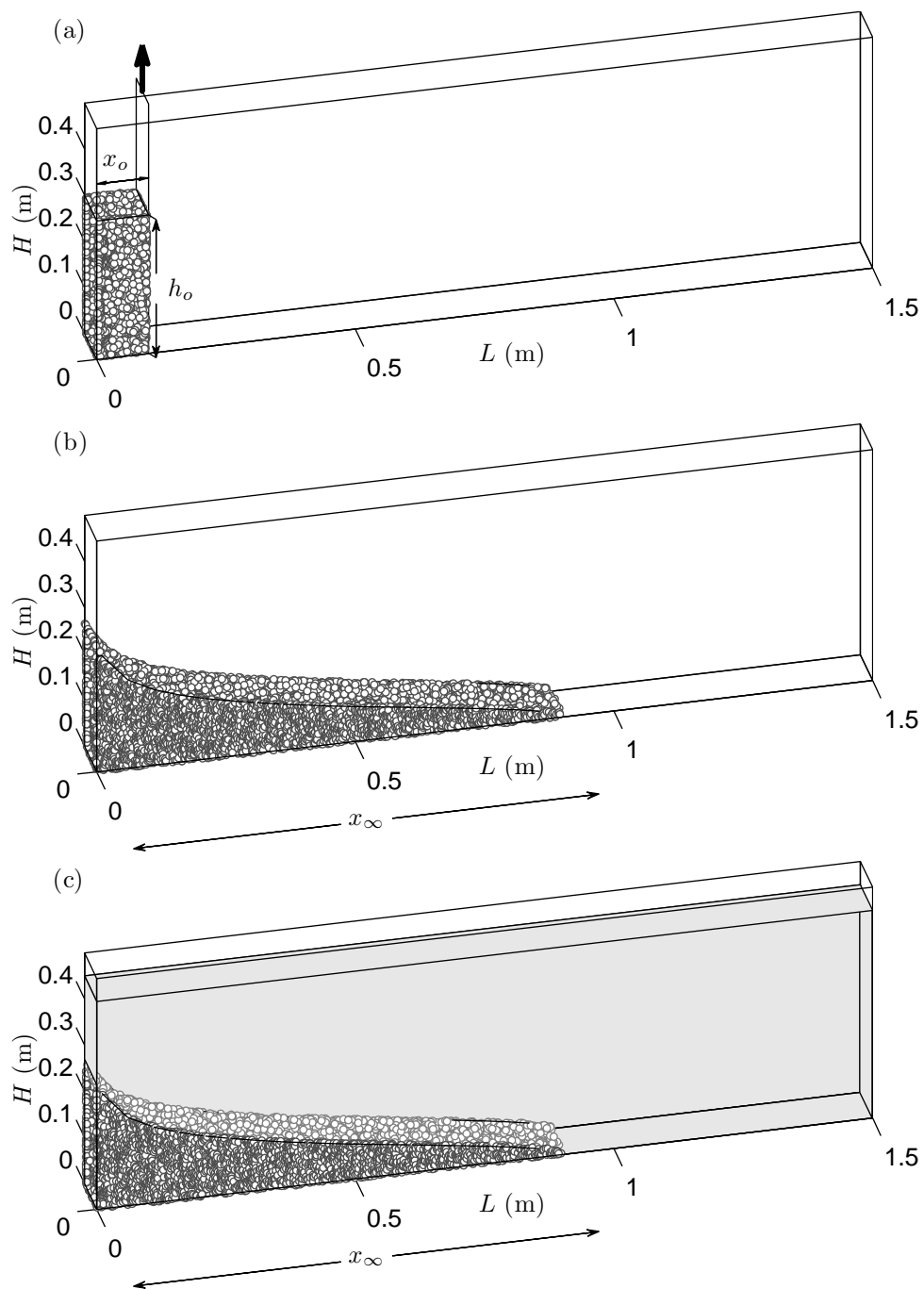
FIGURE 3.1. Experimental facility, perspex rectangular channel of 1.5 m-long, 0.5 m-deep and 0.1 m-wide. (a) Initial experimental set up with a column of grains of aspect ratio h_o/x_o. (b,c) Sketch of the final deposits in air (b) and in water (c).

Set	γ_f (kg m^{-3})	ν_f ($\times 10^{-5}$ m^2 s^{-1})	d_s ($\times 10^{-3}$ m)
1	1.2	1.7	3.0
2	1.2	1.7	0.7
3	1.2	1.7	0.2
4	1000	0.1	3.0
5	1000	0.1	0.7
6	1000	0.1	0.2

TABLE 3.1. Mean values of material properties and boundary conditions for laboratory and numerical experiments of monosized mixtures. For each set: γ_1=2.5×10^3 kg m^{-3}, c=0.6, e=0.95, φ=26°, x_o=0.1 m for $h_o/x_o \in [1, 4.5]$, x_o=0.05 m for $h_o/x_o \in [5, 16]$, $\Delta x = \Delta y$=7.14×10^{-3} m, and Δt=2.5×10^{-3} s.

Set	(d_1 , d_2) ($\times 10^{-3}$ m)	d_1/d_2	γ_f (kg m^{-3})	ν_f ($\times 10^{-5}$ m^2 s^{-1})
A1	(0.2 , 3.0)	0.067	1.2	1.7
B1	(0.7 , 3.0)	0.233	1.2	1.7
A2	(0.2 , 3.0)	0.067	1000	0.1
B2	(0.7 , 3.0)	0.233	1000	0.1

TABLE 3.2. Laboratory and numerical experiments of binary mixtures in air and water. For each set: γ_1=γ_2=2.5×10^3 kg m^{-3}, φ_1=φ_2=26°, c=0.6, x_o=0.1 m for $h_o/x_o \in [1, 4]$, x_o=0.05 m for $h_o/x_o \in [5, 8]$, $\Delta x = \Delta y$=7.14×10^{-3} m, and Δt=2.5×10^{-3} s

voids between the large particles are not filled, different proportions of small and large particles were achieved by varying the height of the column of large particles (h_2 in table 3.3), and filling at different levels (h_1 in table 3.3) the interstices between them (without forcing the large particles apart) as indicated in table 3.3.

The experimental procedure can be summarised as follow. The glass beads were poured into the reservoir without agitation or vibration. The channel was illuminated with diffuse back lighting that provided a good contrast for video analysis, and a video camera was carefully aligned along the horizontal direction. The gate was then manually removed to release the granular mass that spread into the horizontal channel until it came to rest, while the flow was recorded with the video camera at 50 frames per second. Finally, the movie was processed with Matlab® in order to obtain series of the free surface and of the front position of the granular flow.

As the effect of gate removal was not considered in the numerical simulations, we verified the time of opening and found that it was ~ 0.1 s, which was less than about 5 and 10 % of the typical flow duration in water and air, respectively. Furthermore, the error in the front velocity was ± 0.05 m s^{-1}, which corresponded to less than about 4 and 8 % of the typical flow front velocity in air and water, respectively.

Sets	Experiment	h_1	h_2	$\% \; small$
A1 and A2	1	-	h_o	0
	2	$1/3h_o$	h_o	11
	3	$2/3h_o$	h_o	20
	4	h_o	h_o	27
	5	h_o	$2/3h_o$	47
	6	h_o	$1/3h_o$	70
	7	h_o	-	100
B1 and B2	1	h_o	h_o	25
	2	h_o	h_o	50
	3	h_o	h_o	75
	4	h_o	-	100

TABLE 3.3. Experimental set up for initial columns of experiments listed in table 3.2. h_1 and h_2 are the column height of small and large grains, respectively, and
$\% \; small \equiv 100(h_o x_o)^{-1} \int_0^{h_o} \int_0^{x_o} (c_1/[c_1 + c_2])_{t=0} \, dxdy.$

3.2. Numerical solution

Before discussing the numerical solution, two important properties of the systems of non-linear second order partial differential equations (2.25)-(2.27) and (2.47)-(2.49) should be noted. First, as in the case of Navier-Stokes equations, it is not possible to define whether the hyperbolic or parabolic feature of the momentum equations dominates, since the ratio between the rate of convection of the flow to its rate of diffusion (the Péclet number) is not known a priori. Then, the discretisation method should handle both convection and diffusion terms as a unit (Patankar 1980, pp. 79–80). Second, the inviscid limit of these equations, in which momentum losses are not considered, gives an ill-posed system of equations because some wave celerities acquire complex values, i.e. the inviscid equations are non-hyperbolic, and the numerical solution shows that small-scale phenomenon grows rapidly (Drew 1983; Stewart & Wendroff 1984; Ystrom 2001). Then, viscous terms should be retained in order to have a well-posed system of equations (Drew 1983; Ystrom 2001).

Based on this and on the fact that the pressure fields for each constituent are not known, we chose the implicit finite volume pressure-correction scheme proposed by Patankar (1980) for solving the momentum equations of each constituent, which is an iterative procedure for calculating the flow field in a way that improves the guessed pressure. This procedure is based on the fact that the pressure field is indirectly specified via the mass continuity equation, so that when the correct pressure field is substituted into the momentum equations, the resulting velocity field satisfies the mass continuity equation (Patankar 1980, pp. 124–126). In order to prevent numerical instabilities of the velocity field associated to the central difference approximations, the convection and diffusion fluxes were solved with the hybrid scheme, which is a combination of the cen-

tral difference and upwind schemes, and depends on the Péclet number (Patankar 1980, pp. 88–90). Furthermore, we adopted a closed two-dimensional (vertical-longitudinal) domain with a staggered Cartesian grid, in which the velocity components are calculated for the points lying on the faces of the control volumes, which allows avoiding the difficulties that arise when pressure and velocity fields are calculated at the same location, such as non uniform pressure field (Patankar 1980, pp. 118–120).

Regarding to the boundary conditions, a zero mass flow across the walls was considered for both fluid and solids constituents because the domain was closed, so that a normal velocity equal to zero was given as a boundary condition to both the pressure-correction and the momentum equations. Additionally, the non-slip boundary condition was considered for the fluid, so that the fluid velocity parallel to the walls was equal to zero; and a zero momentum flux across the walls was assumed for the solid constituents, so that the gradient of the solids velocity parallel to the walls was equal to zero, which means that solid particles can slip on the walls. Moreover, a wall friction equal to the inner Coulomb friction $\tan\varphi$ was assumed. Finally, as both mean and fluctuating fluid velocities were zero at the walls, the turbulent kinetic energy, k, was also zero at the walls; in contrast, the dissipation rate ϵ should have been finite (Rodi 1983, pp. 44–45). The usual way to treat the boundary conditions for ϵ is by placing the boundaries out of the viscous wall boundary layer, where the flow is fully turbulent, and assuming that the rate of production and dissipation of k are equal in that point, which also required to know the flow velocity in that point (Rodi 1983, pp. 44–45). The same methodology is no longer valid for multi-species flows because there is not a clear definition of the wall viscous boundary layer within the grains; then, we decided to impose $\epsilon = 0$ at the boundary. Note that no specific treatment of the free surface boundary conditions of the granular flow is required, because the proposed granular pressure closure (2.28) naturally creates interfaces as it induces the fall of the particles while the flow is not packed, and because the properties of each constituent vary in space according to the volume fraction.

The final discretised equations are detailed in the Appendix, for which the solution algorithm for one time step can be summarised as follows. (i) Start the calculation of the fields at the new time step with the solution of the previous time step. (ii) Solve the discretised momentum equations for the fluid. (iii) Solve the discretised momentum equations for the small particles. (iv) Solve the discretised momentum equations for the large particles. (v) Solve the pressure-correction equation for the fluid, and correct fluid pressure and velocities (underrelaxed). (vi) Solve the pressure-correction equation for the small particles, and correct solid pressure and velocities (underrelaxed). (vii) Solve the pressure-correction equation for the large particles, and correct solid pressure and velocities (underrelaxed). (viii) Solve the discretised conservation of mass equation for

the small particles. (ix) Solve the discretised conservation of mass equation for the large particles. (x) Solve the discretised $k-\epsilon$ equations for the fluid. (xi) With the new fields, return to step (ii) until a converged solution for both the continuity and momentum equations is satisfied to an acceptable tolerance (difference in velocity between two successive iterations less than 1 mm s^{-1}) for each constituent.

We solved numerically the sets of experiments presented in tables 3.1 and 3.2. The horizontal dimension of the computational domain, L, was given by the experimental facility (i.e. L=1.5 m); whereas, the vertical dimension, H, was chosen as $H = 2h_o$, as we verified that for H larger than $\sim 1.5h_o$ the influence of the boundary condition at the top of the computational grid was negligible. For simplification and because the horizontal dimension of the domain was fixed, independently of the experiment, we used a fixed grid size of $\Delta x = \Delta y$=7.14×10^{-3} m (i.e. $L/\Delta x$=210), and a time step of Δt=2.5×10^{-3} s (i.e. $\sqrt{Lg^{-1}}/\Delta t$=156), such as $\Delta x/\Delta t$=2.9 m s^{-1} was about twice the maximum front propagation speed. The details of the numerical set up for each simulation are also summarised in tables 3.1 and 3.2.

Chapter 4

Dimensionless form of the governing equations

4.1. Characteristics scales and dimensionless variables

We used the governing equations for studying the collapse and spreading of two-dimensional granular columns in air or water, for different binary mixtures of small and large spherical particles of equal mass density and surface roughness (i.e $\varphi_{12} = \varphi_1 = \varphi_2 = \varphi$). Previous experimental studies with monosized grains in air (e.g. Lajeunesse *et al.* 2005; Lube *et al.* 2005) have established that the characteristic time scale is $\sqrt{h_o/g}$, independent of the properties of the granular material (grain size, roughness and shape) and of the initial column aspect ratio h_o/x_o, where h_o and x_o are the initial height and length, respectively. As we also apply the equations in cases in which water is the ambient fluid, we define $T = \sqrt{h_o/g'}$ as the characteristic time scale, where $g' = (\gamma_1 - \gamma_0)/\gamma_1 g$ is the reduced gravity. On the other hand, the traditional dam-break problem for flows of water indicates that the characteristic horizontal velocity scale is the gravity wave celerity $U = \sqrt{g'h_o}$ (von Karman 1940), so that the characteristic horizontal length scale is $\sim UT \sim h_o$. In order to have each term of the same order in the conservation of mass equation, U and h_o are also chosen as scales for both vertical velocity and length. Using the loose packing density of the mixture, $c^*\gamma_1$, (where c^* is the loose solid volume fraction of the mixture, equation 2.50) and the material density of the fluid, γ_0, as density scales, then the following dimensionless variables are obtained:

$$\widetilde{t} = t\sqrt{\frac{g'}{h_o}}, \ \widetilde{x}_i = \frac{x_i}{h_o}, \ \widetilde{u}_{\alpha i} = \frac{u_{\alpha i}}{\sqrt{g'h_o}}, \ \widetilde{u}_{0i} = \frac{u_{0i}}{\sqrt{g'h_o}}, \ \widetilde{\rho}_\alpha = \frac{\rho_\alpha}{c^*\gamma_1}, \ \widetilde{\rho}_0 = \frac{\rho_0}{\gamma_0},$$

$$\widetilde{p}_\alpha = \frac{p_\alpha}{c^*\gamma_1 g'h_o}, \ \widetilde{p}_0 = \frac{p_0}{\gamma_0 g'h_o}, \ \widetilde{p}_c = \frac{p_c}{c^*\gamma_1 g'h_o}, \ \widetilde{k} = \frac{k}{g'h_o}, \ \widetilde{\epsilon} = \frac{\epsilon}{g'h_o}, \ \widetilde{T} = \frac{T}{g'h_o}, \tag{4.1}$$

where $x_1 = x$, $x_2 = y$ are the horizontal and vertical directions, respectively, $\sim$ denotes scaled variables, and the sub-index α=1,2 denotes small and large particles, respectively.

4.2. Dimensionless form of the two-phase equations

The dimensionless form of the two-phase equations for compressible granular flows of monosized grains, is obtaining by substituting the dimensionless variables (4.1) in the conservation of mass (2.25), and momentum equations (2.26) and (2.27):

$$\frac{\partial \widetilde{\rho}_\alpha}{\partial \widetilde{t}} + \frac{\partial (\widetilde{\rho}_\alpha \widetilde{u}_{\alpha i})}{\partial \widetilde{x}_i} = 0, \quad \alpha = 0,1 \tag{4.2}$$

$$\frac{\partial \widetilde{\rho}_0 \widetilde{u}_{0i}}{\partial \widetilde{t}} + \frac{\partial (\widetilde{\rho}_0 \widetilde{u}_{0j} \widetilde{u}_{0i})}{\partial \widetilde{x}_j} = \widetilde{\rho}_0 \frac{g_i}{g'} + \frac{\partial}{\partial \widetilde{x}_j}\left[\frac{1}{Re}\left(\frac{\partial \widetilde{u}_{0i}}{\partial \widetilde{x}_j} + \frac{\partial \widetilde{u}_{0j}}{\partial \widetilde{x}_i}\right)\right] - c_0 \frac{\partial \widetilde{p}_0}{\partial \widetilde{x}_i}$$
$$- \sqrt{\frac{1}{DeAr_1}\frac{h_o}{d_1}}\widetilde{K}_1(\widetilde{u}_{0i} - \widetilde{u}_{1i}), \tag{4.3}$$

$$\frac{\partial \widetilde{\rho}_1 \widetilde{u}_{1i}}{\partial \widetilde{t}} + \frac{\partial (\widetilde{\rho}_1 \widetilde{u}_{1j} \widetilde{u}_{1i})}{\partial \widetilde{x}_j} = \widetilde{\rho}_1 \frac{g_i}{g'} - \frac{\partial \widetilde{p}_1}{\partial \widetilde{x}_i} + s_{ij}\frac{\partial \widetilde{p}_1}{\partial \widetilde{x}_j}\tan\varphi + \frac{\partial}{\partial \widetilde{x}_j}\left[\frac{1}{Re_c}\left(\frac{\partial \widetilde{u}_{1i}}{\partial \widetilde{x}_j} + \frac{\partial \widetilde{u}_{1j}}{\partial \widetilde{x}_i}\right)\right]$$
$$- \frac{\partial \widetilde{p}_c}{\partial \widetilde{x}_i} - De\frac{c_1}{c}\frac{\partial \widetilde{p}_0}{\partial \widetilde{x}_i} + \sqrt{\frac{De}{Ar}\frac{h_o}{d_1}}\frac{\widetilde{K}_1}{c}(\widetilde{u}_{0i} - \widetilde{u}_{1i}), \tag{4.4}$$

where $\widetilde{K}_1 = 3/4(0.63\sqrt{Re_{d1}} + 4.8)^2 c_1 c_0^{1-\zeta_1}$. The density number, De, the Archimedes number, Ar_1, and the Reynolds numbers, Re_c and Re_0, are defined as

$$De = \frac{\gamma_0}{\gamma_1}, \quad Ar_1 = \frac{(\gamma_1 - \gamma_0)gd_1^3}{\gamma_0 \nu_0^2}, \quad Re_c = \frac{c\gamma_1 h_o\sqrt{g'h_o}}{\mu_c}, \quad Re_0 = \frac{\gamma_0 h_o\sqrt{g'h_o}}{\mu_0 + \mu_T}. \tag{4.5}$$

4.3. Dimensionless form of the three-species equations

The dimensionless form of the three-species equations for binary mixtures of small and large grains of equal mass density in a dense regime, is obtaining by substituting the dimensionless variables (4.1) in the conservation of mass (2.47), and momentum equations (2.48) and (2.49):

$$\frac{\partial \widetilde{\rho}_\alpha}{\partial \widetilde{t}} + \frac{\partial (\widetilde{\rho}_\alpha \widetilde{u}_{\alpha i})}{\partial \widetilde{x}_i} = 0, \quad \alpha = 0, 1, 2, \tag{4.6}$$

$$\frac{\partial \widetilde{\rho}_0 \widetilde{u}_{0i}}{\partial \widetilde{t}} + \frac{\partial (\widetilde{\rho}_0 \widetilde{u}_{0j} \widetilde{u}_{0i})}{\partial \widetilde{x}_j} = \widetilde{\rho}_0 \frac{g_i}{g'} + \frac{\partial}{\partial \widetilde{x}_j} \left[\frac{1}{Re} \left(\frac{\partial \widetilde{u}_{0i}}{\partial \widetilde{x}_j} + \frac{\partial \widetilde{u}_{0j}}{\partial \widetilde{x}_i} \right) \right] - c_0 \frac{\partial \widetilde{p}_0}{\partial \widetilde{x}_i}$$
$$- \sum_{\beta=1}^{2} \sqrt{\frac{1}{De Ar_\beta} \frac{h_o}{d_\beta}} \widetilde{K}_\beta (\widetilde{u}_{0i} - \widetilde{u}_{\beta i}), \tag{4.7}$$

$$\frac{\partial \widetilde{\rho}_\alpha \widetilde{u}_{\alpha i}}{\partial \widetilde{t}} + \frac{\partial (\widetilde{\rho}_\alpha \widetilde{u}_{\alpha j} \widetilde{u}_{\alpha i})}{\partial \widetilde{x}_j} = \widetilde{\rho}_\alpha \frac{g_i}{g'} - (1 - c_\beta) \frac{\partial \widetilde{p}_\alpha}{\partial \widetilde{x}_i} + (s_{\alpha ij} - s_{\beta \alpha ij} c_\beta) \frac{\partial \widetilde{p}_\alpha}{\partial \widetilde{x}_j} \tan \varphi - De \frac{c_\alpha}{c^*} \frac{\partial \widetilde{p}_0}{\partial \widetilde{x}_i}$$
$$+ \sqrt{\frac{De}{Ar_\alpha} \frac{h_o}{d_\alpha}} \frac{\widetilde{K}_\alpha}{c^*} (\widetilde{u}_{0i} - \widetilde{u}_{\alpha i}) - c_\alpha \frac{\partial \widetilde{p}_\beta}{\partial \widetilde{x}_i} - s_{\beta \alpha ij} c_\alpha \frac{\partial \widetilde{p}_\beta}{\partial \widetilde{x}_j} \tan \varphi, \quad \alpha \neq \beta = 1, 2, \tag{4.8}$$

where $\widetilde{K}_\alpha = 3/4(0.63\sqrt{Re_{d\alpha}} + 4.8)^2 c_\alpha c_0^{1-\zeta_\alpha}$, and the Archimedes number, Ar_α, is now defined as

$$Ar_\alpha = \frac{(\gamma_1 - \gamma_0) g d_\alpha^3}{\gamma_0 \nu_0^2}, \quad \alpha = 1, 2. \tag{4.9}$$

Chapter 5

Results

5.1. Results of the two-phase model equations

In this section, the two-phase approach (4.2) - (4.3) is used to study the dynamics of homogeneous granular flows and their ambient fluid effects.

5.1.1. *Dynamics of the granular column collapse and spreading*

In order to characterise the particular dynamics of the granular column collapse and spreading, we present in figures 5.1 to 5.3 the results of laboratory experiments and numerical simulations carried out in air or in water with grains size of 3 mm in diameter and columns with $h_o/x_o = 3$.

Figures 5.1 (a,f) show frames of the dimensionless solid pressure, $\widetilde{p}_1$, the streamlines of the granular flow, and a comparison of measured and computed, $c^{-1} \int_0^{\widetilde{H}} c_1(\widetilde{x}, \widetilde{y}) d\widetilde{y}$, free surface of the granular flow, for three dimensionless times $\widetilde{t}$. Figure 5.1 (g) compares time series of $\widetilde{p}_1$ at the left bottom corner of the column and the column height at the left top, y^t/h_o. Finally, a comparison between measured and simulated time series of the dimensionless front position, $(x_F - x_o)/h_o$, is shown in figure 5.1 (h). Figure 5.1 illustrates the mechanisms of the granular collapse. The granular flow is first driven by the horizontal solid pressure gradient; however, the wall boundary condition curves the streamlines and tilts the isobars, inducing the fall of the top of the column where solid pressure is equal to zero (figures 5.1a and 5.1d). The vertical collapse progressively increases the solid pressure at the base of the column (figure 5.1g), thus transferring vertical to horizontal solid phase momentum (figures 5.1b and 5.1e). As a consequence, the flow is mostly non-hydrostatic since $\widetilde{p}_1$ is different than y^t/h_o (figure 5.1g). Finally, the granular motion ends in a static state because of the Mohr-Coulomb condition (figures 5.1c, 5.1f, and 5.1h).

Figure 5.2 shows contour graphs of the dimensionless solid and fluid velocities, $\widetilde{\boldsymbol{u}}_1$ and $\widetilde{\boldsymbol{u}}_0$, kinetic energy of the fluid turbulent motion, $\widetilde{k}$, and granular temperature, $\widetilde{T}$, in air at $\widetilde{t}$=1.5 (left hand panels) and in water at $\widetilde{t}$=2.0 (right hand panels). It is observed static and dynamic regions of the granular flow because of the Mohr-Coulomb condition (figures 5.2a and 5.2b), with a surface above which material slides down and below which grains remain almost static, while in the front area the movement can be described as
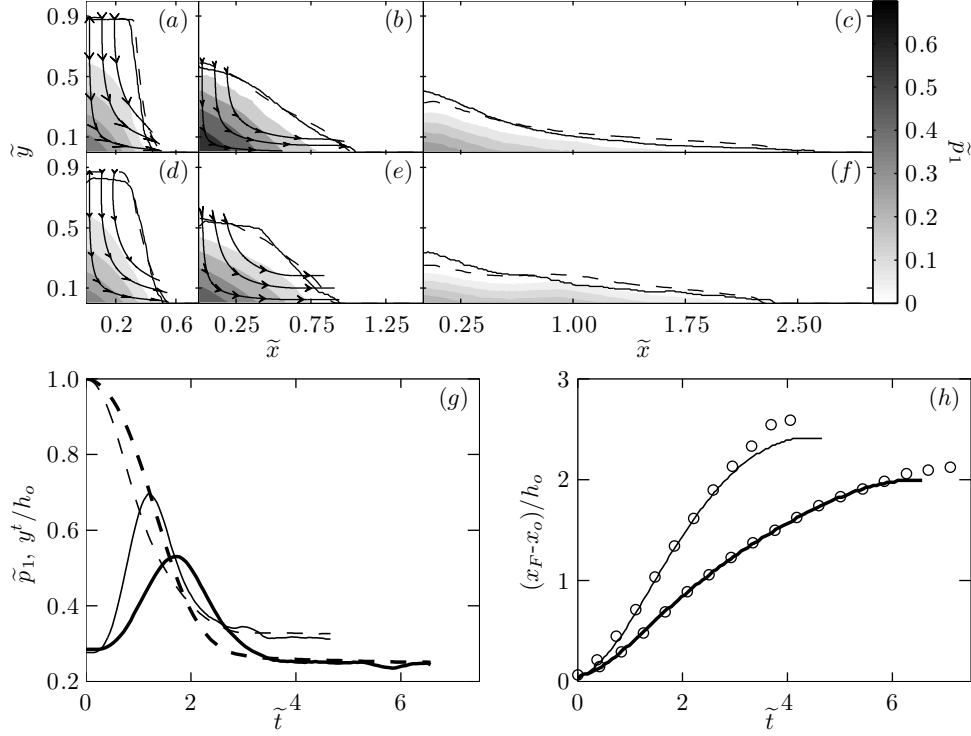
FIGURE 5.1. Frames of $\widetilde{p}_1$ (contours), streamlines of the granular flow ($\rightarrow\rightarrow$), and experimental (———) and computed $c^{-1}\int_0^{\widetilde{H}} c_1(\widetilde{x},\widetilde{y})d\widetilde{y}$ ($---$) free surface, for the collapse of grain columns with d_1=3 mm and h_o/x_o=3 in air at (a) $\widetilde{t}$=0.5, (b) $\widetilde{t}$=1.0, (c) $\widetilde{t}$=3.0, and in water at (d) $\widetilde{t}$=0.75, (e) $\widetilde{t}$=1.5, (f) $\widetilde{t}$=6.0. (g) Time series of $\widetilde{p}_1$ at the left bottom corner of the column (———), and column height y^t/h_o at the left top ($---$), in air (light lines) and in water (dark lines). (h) Comparison between simulated (———) and measured (O) time series of $(x_F - x_o)/h_o$, in air (light line) and in water (dark line).

a plug-like flow. Furthermore, the movement of the surrounding fluid is induced by the solid particles through two mechanisms: drag interactions and volume interchanges. On the one hand, the drag force induces about the same fluid velocity as the solid particles (magnitude and direction), except at the walls where the fluid velocity is constrained by the no-slip fluid boundary condition (figures 5.2c and 5.2d). On the other hand, because of the volume continuity ($c_1 + c_0 = 1$), the ambient fluid occupies the space left by the solid particles, thus generating the large fluid recirculation patterns shown in figures 5.2c and 5.2d. Finally, fluid turbulence is generated in the whole granular flow and is transported by the fluid to zones where there are no solid particles (figures 5.2e and 5.2f), whereas granular temperature is generated mainly at the free surface of the granular flow (figures 5.2g and 5.2h). As a consequence, the eddy viscosity of the fluid phase, μ_T, acts in a much larger volume than the collisional viscosity of the solid phase, μ_c, so that fluid turbulence is expected to be more important than particles collisions, although $Re_0 \sim Re_c \sim 100$.
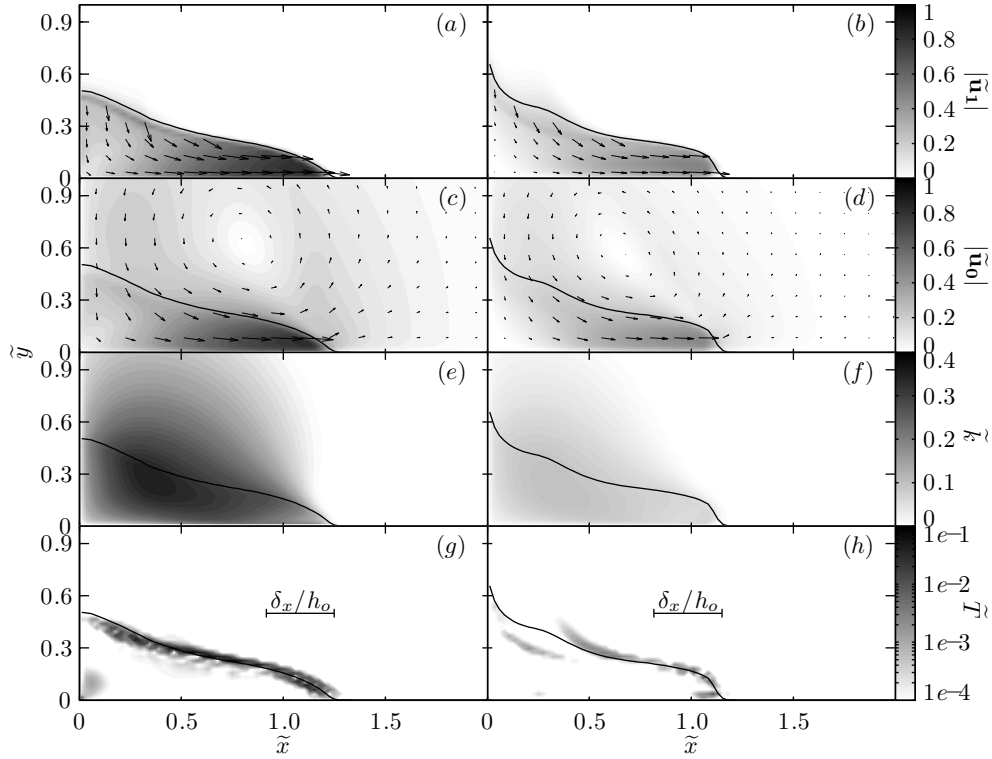
FIGURE 5.2. Numerical results of grain columns with $d_1=3$ mm and $h_o/x_o=3$ in air at $\widetilde{t}=1.5$ (left panels) and in water at $\widetilde{t}=2.0$ (right panels). Spatial variation of the magnitude (contour) and direction (arrows) of $\widetilde{u}_1$ (*a,b*) and of $\widetilde{u}_0$ (*c,d*). Contour graph of $\widetilde{k}$ (*e,f*) and of $\widetilde{T}$ (*g,h*), and horizontal dimensions of CV, $\delta_x/h_o = 0.3$ (*g,h*). The black solid line represents the dimensionless free surface of the granular flow, $c^{-1}\int_0^{\widetilde{H}} c_1(\widetilde{x},\widetilde{y})d\widetilde{y}$.

The dimensionless front position in figure 5.3 (*a,b*) shows the well known acceleration, constant velocity, and deceleration regimes, which characterise the dynamics of granular column collapses (e.g. Lajeunesse *et al.* 2005; Lube *et al.* 2005). To understand the constant velocity regime, the force balance at the front was studied by integrating (4.4) in the Lagrangian control volume, CV, defined between $\widetilde{x} = (x_F - \delta_x)/h_o$ and $\widetilde{x} = x_F/h_o$, and the whole vertical domain (δ_x is shown in figures 5.2*g* and 5.2*h*, and $\delta_x/h_o = 0.3$). The horizontal solid phase momentum equation (4.4) was written for the Lagrangian coordinates $\widetilde{t}' = \widetilde{t}$, $\widetilde{y}' = \widetilde{y}$, and $\widetilde{x}' = \widetilde{x} - \widetilde{u}_F\widetilde{t}$, with $\widetilde{u}_F = u_F/\sqrt{g'h_o}$ constant. Figure 5.3 (*c,d*) shows the time series of volume integrated dimensionless terms of the horizontal solid phase momentum equation: Lagrangian momentum advection ($-\partial_{\widetilde{x}'}[\widetilde{\rho}_1(\widetilde{u}_1 - \widetilde{u}_F)\widetilde{u}_1]$), solid pressure gradient ($-\partial_{\widetilde{x}'}\widetilde{p}_1$), Coulomb friction ($s_{xy}\partial_{\widetilde{y}'}\widetilde{p}_1\tan\varphi$), collisional pressure gradient ($-\partial_{\widetilde{x}'}\widetilde{p}_c$), collisional shear stress ($\partial_{\widetilde{x}'}[2Re_c^{-1}\partial_{\widetilde{x}'}\widetilde{u}_1] + \partial_{\widetilde{y}'}[Re_c^{-1}(\partial_{\widetilde{y}'}\widetilde{u}_1 + \partial_{\widetilde{x}'}\widetilde{v}_1)]$), fluid pressure gradient ($-Dec_1/c\partial_{\widetilde{x}'}\widetilde{p}_0$), and drag force ($\sqrt{De\,h_o/(Ar_1\,d_1)}\widetilde{K}_1/c[\widetilde{u}_0 - \widetilde{u}_1]$). Note that because Lagrangian momentum advection is calculated with a constant front speed, this is only valid in the constant velocity regime (shaded areas in figure 5.3).
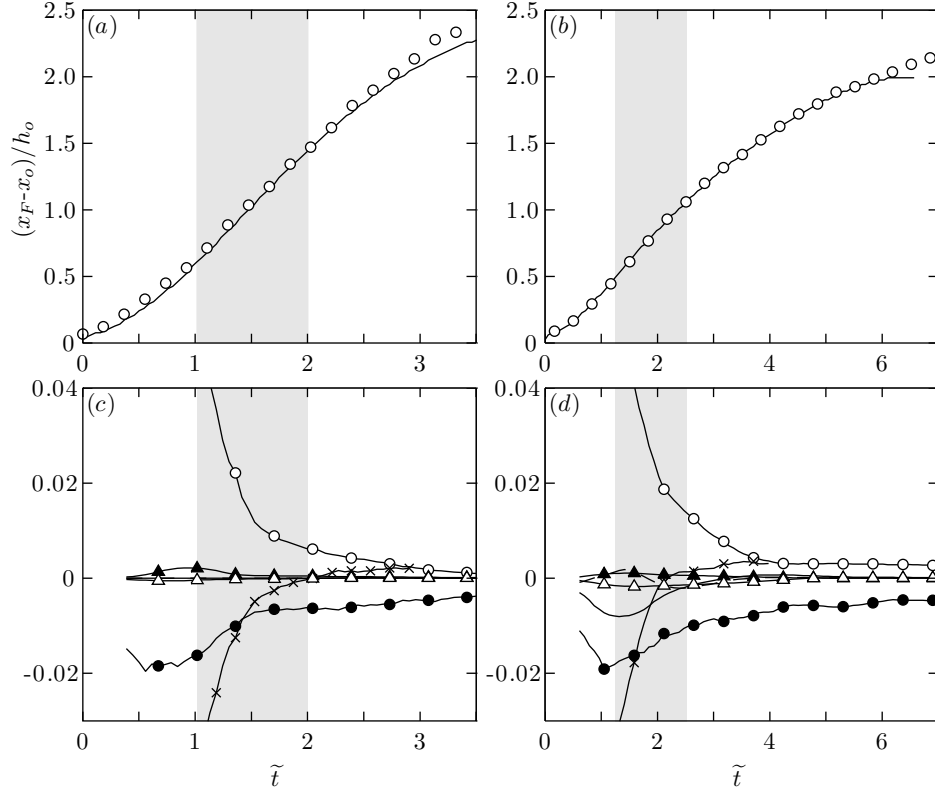
FIGURE 5.3. Results of grain columns with d_1=3 mm and h_o/x_o=3 in air (left panels) and in water (right panels). (a,b) Measured ($\bigcirc$) and simulated (———) time series of $(x_F-x_o)/h_o$. (c,d) Temporal variation of the horizontal forces integrated over CV: advection $-\partial_{\tilde{x}'}[\tilde{\rho}_1(\tilde{u}_1-\tilde{u}_F)\tilde{u}_1]$ (—×—), solid pressure gradient $-\partial_{\tilde{x}'}\tilde{p}_1$ (—$\bigcirc$—), Coulomb friction $s_{xy}\partial_{\tilde{y}}\tilde{p}_1\tan\varphi$ (—●—), collisional pressure gradient $-\partial_{\tilde{x}'}\tilde{p}_c$ (—▲—), collisional shear stress $\partial_{\tilde{x}'}[2Re_c^{-1}\partial_{\tilde{x}'}\tilde{u}_1]+\partial_{\tilde{y}'}[Re_c^{-1}(\partial_{\tilde{y}'}\tilde{u}_1+\partial_{\tilde{x}'}\tilde{v}_1)]$ (—△—), fluid pressure gradient $-Dec_1/c\partial_{\tilde{x}'}\tilde{p}_0$(– – –), and drag force $\sqrt{De\,h_o/(Ar_1\,d_1)}\tilde{K}_1/c[\tilde{u}_0-\tilde{u}_1]$ (———). Shaded areas correspond to the constant velocity regime.

The temporal variation of the horizontal forces integrated over CV shows that the force balance, for the case of the larger particles considered, is described mainly by the balance between horizontal pressure gradient and Coulomb friction (figures 5.3c and 5.3d); however, as shown in the following sections, the relative importance of these forces on the balance changes as a consequence of the particle diameter and fluid properties.

5.1.2. *Role of the solid pressure and Coulomb friction*

In order to identify the solid pressure and Coulomb friction effects on granular flow dynamics, we carried out two types of numerical experiments without both fluid and particles collisions, either with or without Coulomb friction. The results of the dimensionless front speed in the constant velocity regime $u_F/\sqrt{gx_o}$ (with u_F defined as $u_F \equiv max(dx_F/dt)$), as a function of h_o/x_o, are presented in figure 5.4(a). They show

that, as expected from energy considerations, the front speed for the frictionless case is larger than that for the case with friction. Moreover, whereas u_F depends on h_o/x_o for the frictional case (figure 5.4a), $u_F \approx \sqrt{2gh_o}$ in the case without friction, which corresponds to the speed of free fall of the grains from a high h_o. Thus, for the frictionless case, the solid pressure deviates the motion of the granular flow without influencing its speed. As a result, in order to quantify the Coulomb friction effect, we define an equivalent height, h_e, as

$$h_e = h_e(\tan\varphi, h_o/x_o) = \frac{u_F'^2}{2g}, \qquad (5.1)$$

where u_F' refers to the front speed without fluid and particles collisions. The ratio h_e/h_o and the dimensionless runout distance, $(x_\infty - x_o)/x_o$, as a function of h_o/x_o, are shown in figures 5.4 (b) and 5.4 (c), respectively. Both curves show a break in slope at $h_o/x_o \approx 3$, and the runout distance is in quite good agreement with the experimental scaling laws found by Balmforth & Kerswell (2005), Lube *et al.* (2005) and Lajeunesse *et al.* (2005), among others. These numerical experiments show that the physical origin of the break in slope for the dimensionless runout distance is the Coulomb friction ($\tan\varphi$); however, the two-dimensional non-hydrostatic feature of the flow complicates the analysis, so that it is not possible to obtain a direct algebraic expression to compute neither h_e/h_o nor $(x_\infty - x_o)/x_o$ as a function of $\tan\varphi$. Nevertheless, from the numerical results of figure 5.4 (b), we can obtain the following expression:

$$\frac{h_e}{h_o} = \begin{cases} 0.4 & 1 \leqslant h_o/x_o \leqslant 3, \\ 0.76(h_o/x_o)^{-0.58} & 3 < h_o/x_o \leqslant 16, \end{cases} \qquad (5.2)$$

which is valid for the case of monosized glass beads ($\varphi = 26^o$) and $1 \leqslant h_o/x_o \leqslant 16$, and is used in the next sections to subtract the effects of $\tan\varphi$ and h_o/x_o.

5.1.3. *Role of the ambient fluid on granular flow dynamics*

The six sets of experiments summarised in table 3.1 are used for studying the role of the ambient fluid on the granular flow dynamics. We chose the front speed in the constant velocity regime to describe the granular flow because it is more sensitive to the ambient fluid effects. Figure 5.5 (a) shows a comparison of simulated and measured dimensionless front speed, $u_F/\sqrt{g'x_o}$, as a function of h_o/x_o, for the six sets of experiments. A good agreement is observed without fitting any parameter on the model, thus validating the system of governing equations proposed. Furthermore, the results of figure 5.5 (a) suggest that the dependence between u_F and h_o/x_o obtained for the case without fluid is also present when the ambient fluid is considered. This is shown in figure 5.5 (a) with the dashed lines that were obtained by multiplying the results curve obtained without fluid and particles collisions (black solid line) by a factor that
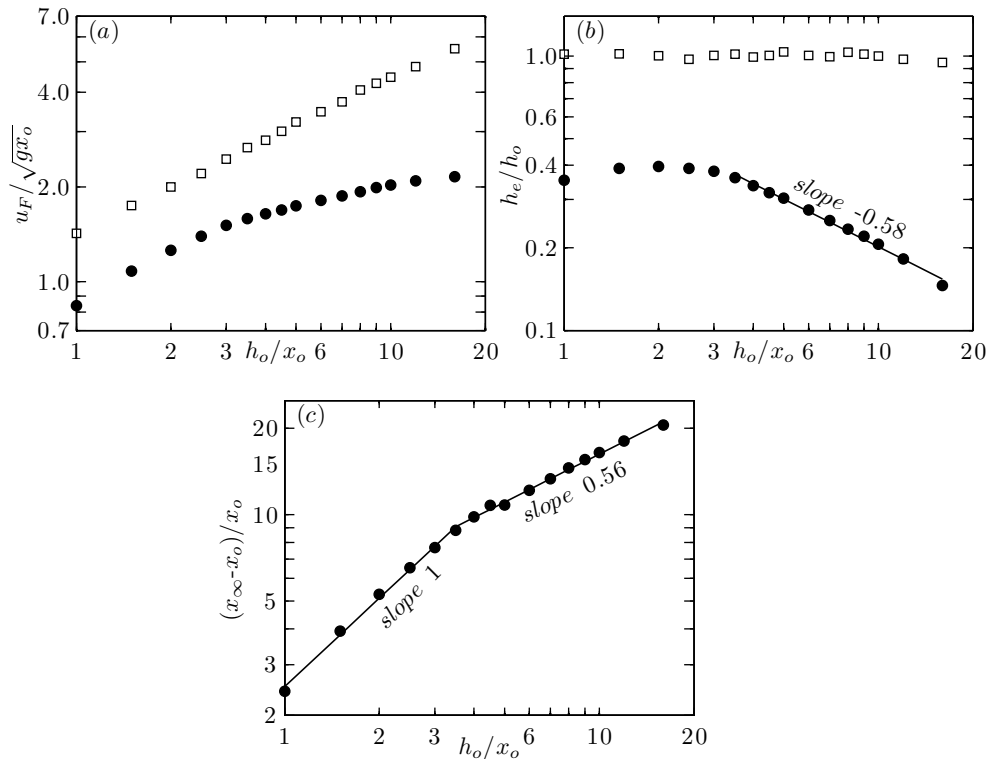
FIGURE 5.4. Results of numerical experiments without fluid and particles collisions. (a) Dimensionless front speed $u_F/\sqrt{gx_o}$ and (b) ratio h_e/h_o, as a function of h_o/x_o, for both sets with ($\bullet$) and without ($\square$) Coulomb friction. (c) Dimensionless runout distance, $(x_\infty - x_o)/x_o$, as a function of h_o/x_o, for the case with Coulomb friction ($\bullet$).

fits each set of experiments. Therefore, the front speed can be written as

$$u_F = Fr\sqrt{2g'h_e}, \tag{5.3}$$

where Fr is a Froude number, and h_e is calculated from the numerical experiments without fluid and particles collisions (5.2). On the other hand, in the dimensional analysis of §4.2, the dimensionless groups that weight the interaction terms of (4.4) were introduced: De, Ar_1, c_1/c, $\sqrt{h_o/d_1}$, and $\widetilde{K}_1/c$. The last three groups depend on the initial and boundary conditions, and from figure 5.5 (a) they are contained in h_e, at least for the laboratory scale considered. Thus, $Fr = Fr(De, Ar_1)$ only depends on the solid particle diameter and fluid properties. Experimental front velocities are used to test this hypothesis, and figure 5.5 (b) shows the best fit curve that relates Fr and one function of De and Ar_1, preserving the physical limits $Fr = 0$ for $\gamma_1 = \gamma_0$, and $Fr = 1$ defined without fluid.

Note that even if the front speed is made dimensionless with g', the ambient fluid effects cannot be restricted to the buoyancy force (figure 5.5), and it is required to analyse the hydrodynamic fluid pressure and drag interactions to characterise accurately
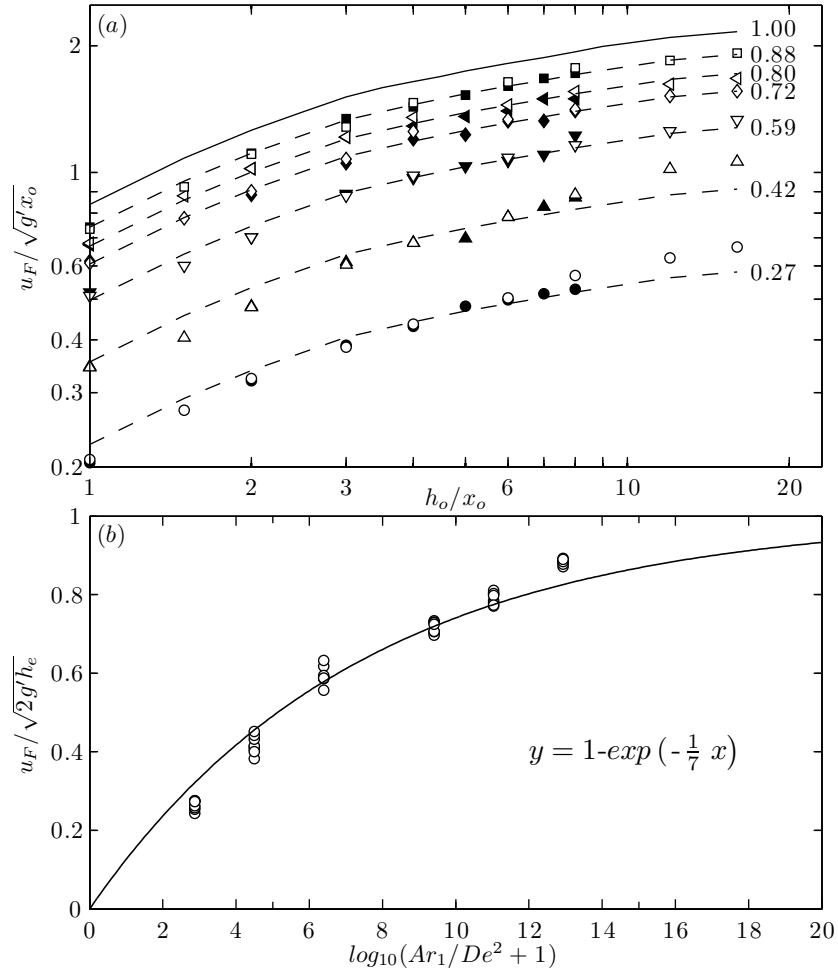
FIGURE 5.5. (*a*) Results of dimensionless front speed, $u_F/\sqrt{g'x_o}$, as a function of h_o/x_o, for experiments of table 3.1: set 1 ($\square$), set 2 ($\triangleleft$), set 3 ($\diamond$), set 4 ($\triangledown$), set 5 ($\triangle$), and set 6 ($\bigcirc$). White and black marks are numerical and experimental results, respectively. The dashed lines were obtained by multiplying the results curve without fluid and particles collisions (———) by the factor indicated. (*b*) Froude number, $Fr = u_F/\sqrt{2g'h_e}$, as a function of $\log_{10}(Ar_1/De^2 + 1)$, for the six sets of experimental measurements of table 3.1 ($\circ$). The best fit is represented by the solid line that preserves the physical limits $Fr = 0$ for $\gamma_1 = \gamma_0$, and $Fr = 1$ defined without fluid.

the role of the ambient fluid on granular flow dynamics. Therefore, it is instructive to examine in more detail the spatial and temporal variation of quantities involved in the balance of forces at the front.

Figure 5.6 shows the results of columns with h_o/x_o=8 and grains of 0.7 mm, in air at $\widetilde{t}$=2.0 (left panels) and in water at $\widetilde{t}$=3.5 (right panels). This figure synthesises the role of the ambient fluid. The grains are not packed at the front (figures 5.6*a* and 5.6*b*) because their weight is held by both hydrostatic and hydrodynamic fluid pressure (figures 5.6*c* and 5.6*d*). Thus, the solid pressure as well as the Coulomb friction is zero in this area (figures 5.6*c* and 5.6*d*). This effect is larger in water than in air, suggesting
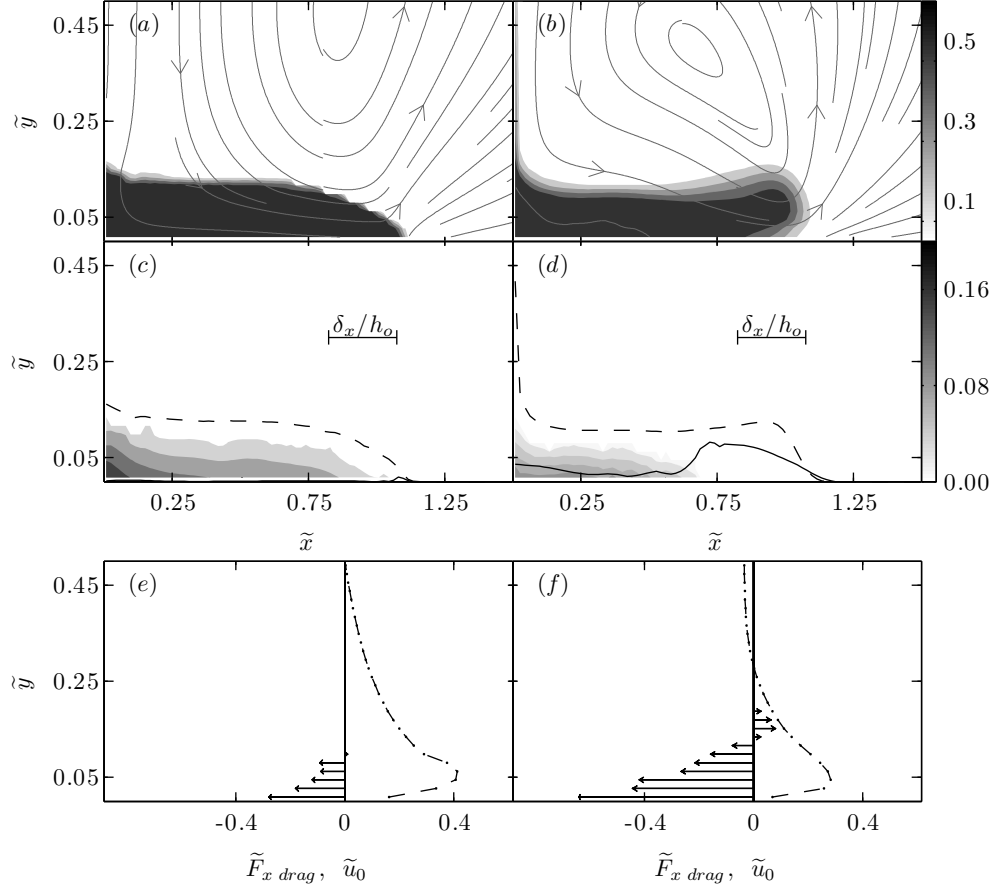
FIGURE 5.6. Numerical results of grain columns with d_1=0.7 mm and h_o/x_o=8 in air at $\widetilde{t}$=2.0 (left panels) and in water at $\widetilde{t}$=3.5 (right panels). (a,b) Contours of c_1 with the streamlines of fluid velocity $(\longrightarrow)$. (c,d) Contours of $\widetilde{p}_1$, computed free surface $c^{-1}\int_0^{\widetilde{H}} c_1(\widetilde{x},\widetilde{y})d\widetilde{y}$ $(---)$, non-hydrostatic fluid pressure at the bottom of the reservoir dimensionless by $c\gamma_1 g'h_o$ $(\underline{\hspace{1.5em}})$, and horizontal dimensions of CV, $\delta_x/h_o = 0.3$. (e,f) Dimensionless drag force $\widetilde{F}_{x\,drag} = \sqrt{De\,h_o/(Ar_1\,d_1)}\widetilde{K}_1/c[\widetilde{u}_0 - \widetilde{u}_1]$ $(\rightarrow)$, and horizontal fluid velocity $\widetilde{u}_0$ $(-\cdot-\cdot)$, profiles in the front area.

that the magnitude of the fluid pressure fluctuations depends on the fluid density, that is, it is described by De. Even when there is no Coulomb friction at the front, the solid phase movement may decelerate, as the increase of fluid pressure is caused by momentum transfer through drag interactions, and because the no-slip fluid boundary condition imposes small speed regions near the walls (figures 5.6e and 5.6f).

Figure 5.7 (a,b) shows measured and simulated time series of $(x_F - x_o)/h_o$, and figure 5.7 (c,d) shows the time series of volume integrated dimensionless terms of the horizontal solid phase momentum equation for the experiments presented in figure 5.6. The temporal variation of the horizontal forces shows that the force balance is described by different interacting forces that depend on the nature of the ambient fluid. In air, the movement is mainly driven by solid pressure gradient, while Coulomb friction (and
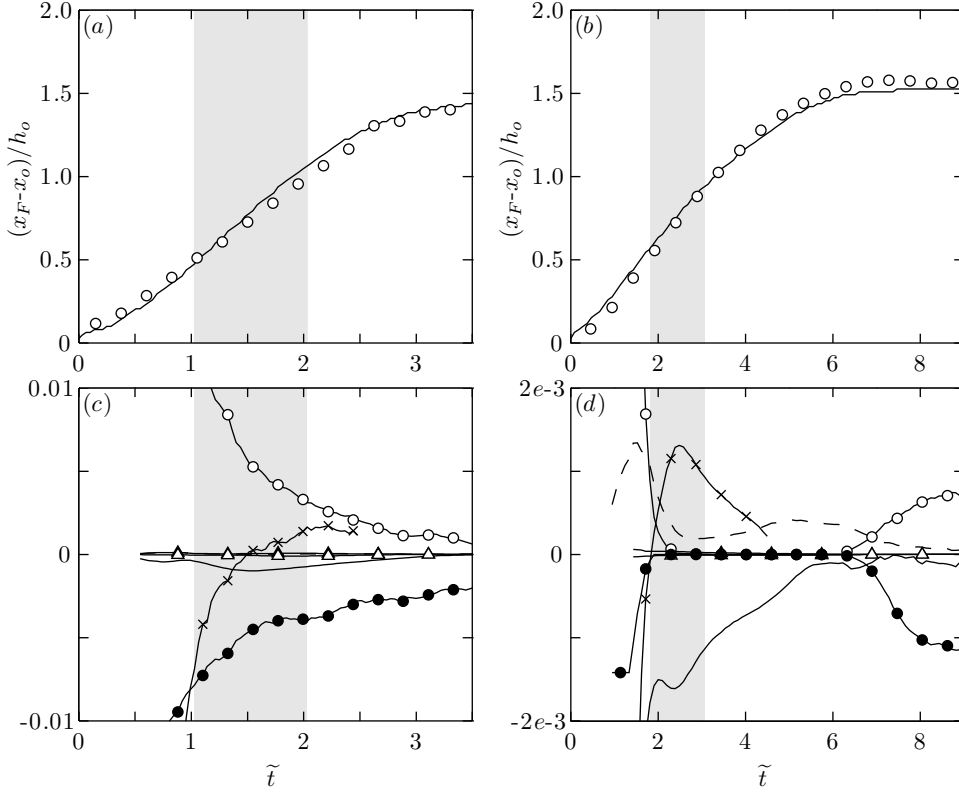
FIGURE 5.7. Results of grain columns with d_1=0.7 mm and h_o/x_o=8 in air (left panels) and in water (right panels). (a,b) Measured ($\bigcirc$) and simulated (——) time series of $(x_F - x_o)/h_o$. (c,d) Temporal variation of the horizontal forces integrated over CV: advection $-\partial_{\tilde{x}'}[\tilde{\rho}_1(\tilde{u}_1 - \tilde{u}_F)\tilde{u}_1]$ (—×—), solid pressure gradient $-\partial_{\tilde{x}'}\tilde{p}_1$ (—$\bigcirc$—), Coulomb friction $s_{xy}\partial_{\tilde{y}'}\tilde{p}_1 tan\varphi$ (—●—), collisional pressure gradient $-\partial_{\tilde{x}'}\tilde{p}_c$ (—▲—), collisional shear stress $\partial_{\tilde{x}'}[2Re_c^{-1}\partial_{\tilde{x}'}\tilde{u}_1] + \partial_{\tilde{y}'}[Re_c^{-1}(\partial_{\tilde{y}'}\tilde{u}_1 + \partial_{\tilde{x}'}\tilde{v}_1)]$ (—△—), fluid pressure gradient $-Dec_1/c\partial_{\tilde{x}'}\tilde{p}_0$(— — —), and drag force $\sqrt{De\ h_o/(Ar_1\ d_1)}\widetilde{K}_1/c[\tilde{u}_0 - \tilde{u}_1]$ (——). Shaded areas correspond to the constant velocity regime.

drag to a lesser extent) counteracts the movement (figure 5.7c). In contrast, the movement in water is mainly driven by momentum advection (and fluid pressure gradient to a lesser extent), while drag counteracts the movement (figure 5.7d). The deceleration phase starts when solid pressure gradient is not large enough against Coulomb friction in air (figure 5.7c), and when advection is not large enough against drag in water (figure 5.7d). In both cases of air and water, the granular motion ends in a static state because of Coulomb friction.

An important issue of the model that deserves a further analysis is the turbulence of the fluid phase, as in both cases of air and water drag forces coupled with the wall fluid viscous effects counteract the solid movement (figures 5.6e and 5.6f), so that near wall viscous effects seem to be important. Figure 5.8 shows a sensitivity analysis of the results for the smallest particles considered comparing simulations with and without fluid turbulence. It is observed that the front speed increases considerably if the fluid
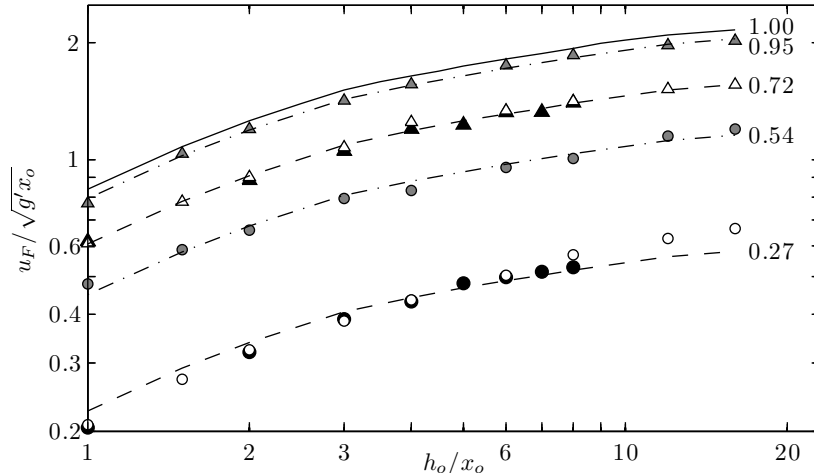
FIGURE 5.8. Results of $u_F/\sqrt{g'x_o}$ as a function of h_o/x_o, for set 3 ($\triangle$) and set 6 ($\bigcirc$) of table 3.1. White and gray marks are numerical results with and without fluid turbulence, respectively, and black marks are experimental measurements. The dashed lines were obtained by multiplying the results curve without fluid and particles collisions (———) by the factor indicated.

turbulence is not considered, with an increase in speed, calculated as $(u_F'' - u_F)/u_F$ with u_F'' being the front speed without turbulence, of about 32% in the case of air and of about 100% in the case of water (figure 5.8). This sensitivity analysis shows that apart from representing accurately the interaction mechanisms between the phases, the dynamic of each phase has to be properly described.

5.2. Results of the three-species model equations

In this section, the three-species approach (4.6) - (4.8) is used to study the dynamics of dense heterogeneous granular flows and their associated segregation effects.

5.2.1. *Validation of the model equations*

To validate the new constitutive relation (2.38) that describes the interactions between solid constituents in a dense regime, we first conducted numerical experiments for the collapse and spreading of a granular column composed by two solid species, named 1 and 2, with equal material density and diameter ($\gamma_1 = \gamma_2$ and $d_1 = d_2$) in a viscous fluid. In this condition, the three-species flow dynamics is identical to the monosized counterpart (i.e., two-phase flows). We carried out these numerical experiments with the larger particles in air (experiment A1.1 of table 2), for which the fluid effects are less important, and we varied the relative solid fractions between $(X_1,X_2) = (0\%,100\%)$, $(25\%,75\%)$ and $(50\%,50\%)$. The results of this analysis are presented in figure 5.9 that also shows a comparison with the experimental measurements. Figures 5.9 (a,b) show frames of the dimensionless solid pressure for the case of $(25\%, 75\%)$, called $\widetilde{p}_1$ and $\widetilde{p}_2$,
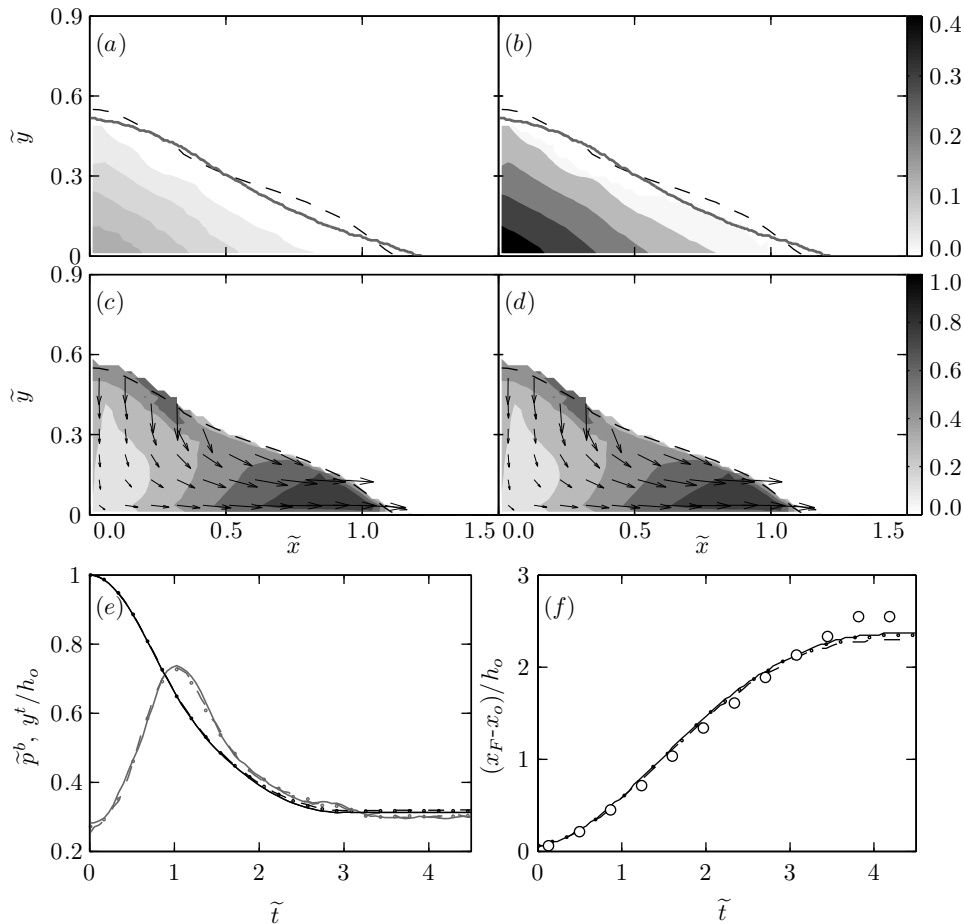
FIGURE 5.9. Results of granular column collapse and spreading in air with grains size of 3 mm and columns with h_o/x_o=3. The numerical experiments were carried out by varying the proportions of the same solid constituent between (0%,100%), (25%,75%) and (50%,50%). (*a-d*) Numerical results of experiment (25%,75%) at $\widetilde{t}$=1.3, in which results for the constituent 1 (X_1=25%) and 2 (X_2=75%) are shown in the left and right panels, respectively. (*a-b*) Contour graphs of the dimensionless solid pressures $\widetilde{p}_1$ and $\widetilde{p}_2$, and experimental (——) and computed $c^{-1}\int_0^{\widetilde{H}}(c_1(\widetilde{x},\widetilde{y}) + c_2(\widetilde{x},\widetilde{y}))d\widetilde{y}$ (– – –) free surface of the granular flow. (*c-d*) Spatial variation of the magnitude (contour) and direction (arrows) of the solid velocities $\widetilde{\boldsymbol{u}}_1$ and $\widetilde{\boldsymbol{u}}_2$. (*e*) Time series of the total solid pressure at the left bottom corner of the column $\widetilde{p}^b = \widetilde{p}_1{}^b + \widetilde{p}_2{}^b$ (gray lines) and the column height at the left top y^t/h_o (black lines), and (*f*) comparison between measured (○) and simulated time series of $(x_F - x_o)/h_o$ for (0%,100%) (——), (25% ,75%)(– · – ·) and (50% ,50%) (– – –).

and a comparison between measured and simulated free surface of the granular flow, where the simulated free surface is defined as $c^{-1}\int_0^{\widetilde{H}}(c_1(\widetilde{x},\widetilde{y}) + c_2(\widetilde{x},\widetilde{y}))d\widetilde{y}$. Figures 5.9 (*c,d*) show contour graphs of the dimensionless solid velocities, called $\widetilde{\boldsymbol{u}}_1$ and $\widetilde{\boldsymbol{u}}_2$, and figure 5.9 (*e*) compares time series of the total solid pressure at the left bottom corner of the column, $\widetilde{p}^b = \widetilde{p}_1{}^b + \widetilde{p}_2{}^b$, and the column height at the left top, y^t/h_o, while figure 5.9*f* compares time series of the dimensionless front position, $(x_F - x_o)/h_o$. Figure 5.9 validates the solid interaction closure (2.38), as the three-constituent simulations give the same numerical results as for the case of a single constituent (figures

5.9e and 5.9f). In particular, the numerical solution shows that the total solid pressure is partitioned accordingly to the relative solid fraction of each component (figures 5.9a and 5.9b), and is equal to the simulated solid pressure for one solid constituent (figure 5.9e). Furthermore, in the three-constituent simulations, both solid components have the same solid velocity (figures 5.9c and 5.9d) and front speed (figure 5.9f), thus preserving the mixture force balance independent of the fractions of the components.

Before validating the constitutive relation (2.38) for the case of binary mixtures of small and large grains, it is necessary to analyse the parameter $\sigma > 0$ introduced in the empirical function $\eta(\sigma)$ of (2.53) in order to address the kinetic sieving of small grains. As in the previous section, the front speed in the constant velocity regime, $u_F = max(dx_F/dt)$, is used as a control parameter in the following analysis. A sensitivity analysis of the front speed depending on σ is presented in figure 5.10a, which shows the ratio between simulated and measured front speed, u_F^s/u_F^m, for experiments A1.4 and B1.1 of table 3.3. It is observed that the simulated front speed is smaller than the experimental measurements when σ=0, and approaches to those measurements when σ increases (figure 5.10a). The effect of σ is explained by the expansion of the granular network induced by the particle segregation. This is shown in figures 5.10 (b,d) by comparing the measured (figure 5.10b) and simulated deposits of A1.4 in cases of σ=1.4 (figure 5.10c) and σ=0.0 (figure 5.10d). Percolation of the small grains induces the segregation of the large particles at the top of the flow (figures 5.10b and 5.10c), which in turns decreases the mixture concentration (see figure 2.2) and increases the mixture volume. This volumetric expansion is then reflected in the front speed, as the kinetic energy is proportional to both the solid concentration and square velocity, so that by conservation of energy a decrease in solid concentration is compensated with an increase in speed.

Using σ=1.4 in (2.53) to model the kinetic sieving of small grains, the four sets of experiments summarised in table 3.2 were simulated and the results for h_o/x_o=3 are presented in Figure 5.11. A good agreement between simulated and measured front speed is observed (figure 5.11a), preserving the same experimental tendency of the front speed depending on the initial relative solid concentration of small grains (the experimental tendency is represented by the dashed lines of figures 5.11b and 5.11c), thus validating the system of governing equations (4.6)-(4.8) for heterogeneous granular flows of binary mixtures of small and large spherical particles in a viscous fluid.
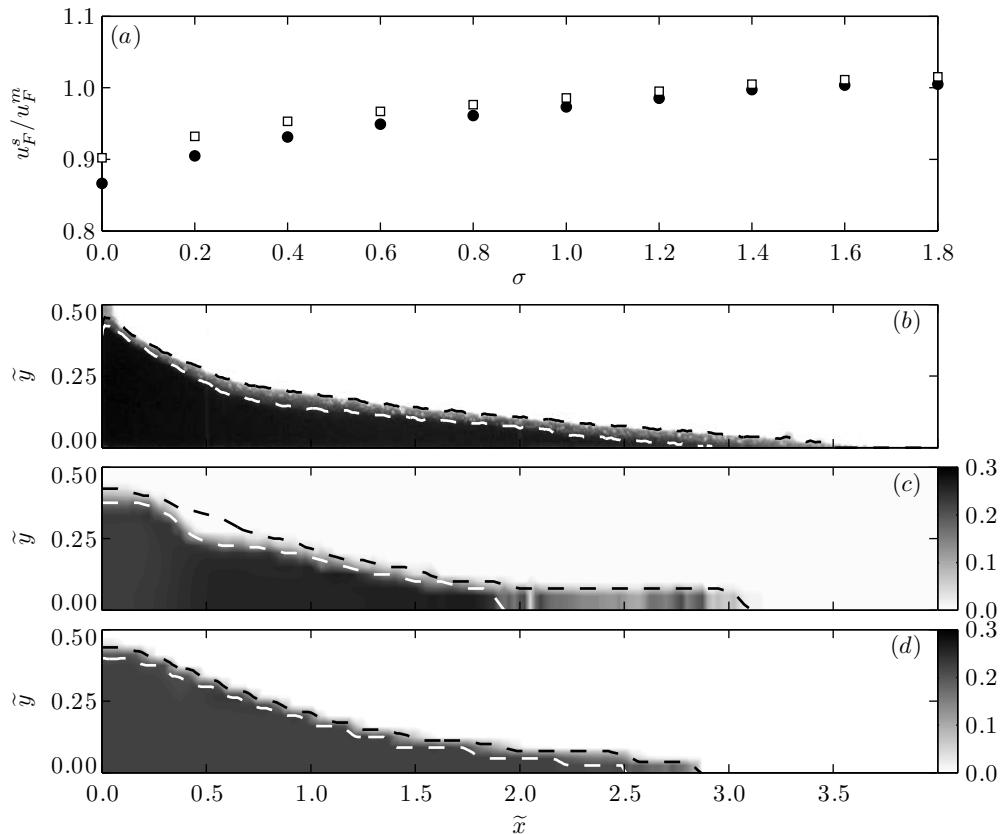
FIGURE 5.10. (*a*) Ratio between simulated and measured front speed, u_F^s/u_F^m, as a function of σ for experiments A1.4 (●) and B1.1 (□) of table 3.3 and h_o/x_o=2. (*b*) Image of the experimental deposit of A1.4. (*c-d*) Contour graph of the solid concentration of small particles, c_1, for simulated deposits of A1.4 with σ=1.4 (*c*) and σ=0.0 (*d*). White dashed line marks the separation between the layer with small and large grains at the bottom of the deposit and the layer rich in large grains at the surface (in where $c_1 <0.1$), and the black dashed line represents the free surface of the deposit.

5.2.2. *On the dynamics of dense heterogeneous granular flows*

In order to verify that the results obtained from experiments with h_o/x_o=3 (figures 5.11*b* and 5.11*c*) are independent of the initial column aspect ratio, we repeated each set of experiments with columns of h_o/x_o=2,3,4,6,8. For comparison of the results, we used $h_e = h_e(\tan\varphi, h_o/x_o)$ of (5.2), introduced in § 5.1.2 to subtract the effects of $\tan\varphi$ and h_o/x_o. Figure 5.12 shows the Froude number, Fr, as a function of the initial volume fraction of small grains for the four sets of experiments of table 3.2. For the case of experiments in air (experiments A1 and B1 in figure 5.12), the front speed increases when the initial volume fraction of small grains increases until $\sim 27\%$ (figure 5.12), which according to (2.50) corresponds to the optimal or maximum packing concentration of the mixture. As discussed in the previous section, this behaviour is caused by the particle segregation that increases the solid mixture volume, and it is more important
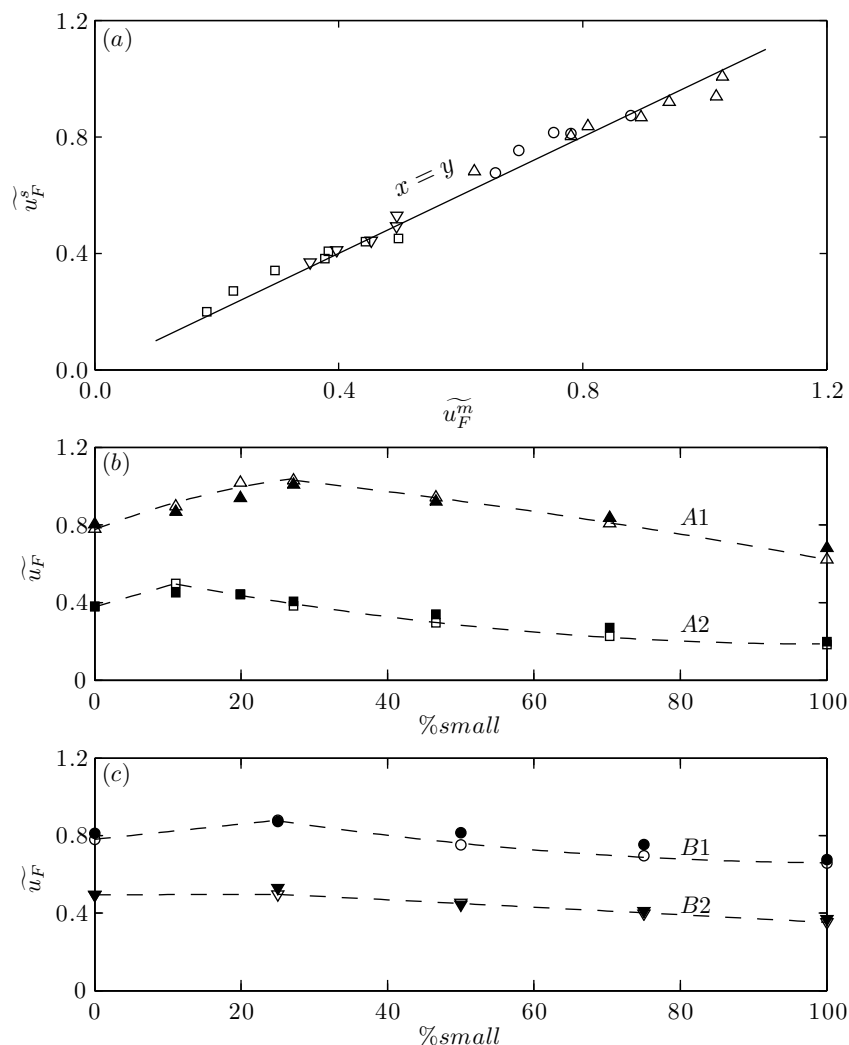
FIGURE 5.11. (a) Simulated, $\widetilde{u_F^s}$, versus modelled, $\widetilde{u_F^m}$, dimensionless front speed for the four sets of experiments of table 3.2 with $h_o/x_o{=}3$ and $\sigma{=}1.4$. (b-c) $\widetilde{u_F}$ as a function of the initial volume fraction of small grains for sets A1 ($\triangle$) and A2 ($\square$) (b), and B1 ($\bigcirc$) and B2 ($\triangledown$) (c). White and black marks are experimental and numerical results, respectively. The experimental tendency is represented by the dashed line.

for binary mixtures with $d_1/d_2{=}0.07{<}0.15$ (experiments A1 in figure 5.12a) than for binary mixtures with $d_1/d_2{=}0.22$ (experiments B1 in figure 5.12b).

When repeating the same experiments in water (curves A2 and B2 in figure 5.12), the increment in front speed due to particle segregation is damped, and the maximum of the front speed is shifted toward the left-hand side of the figure, for which the relative concentration of small grains is smaller (see experiments A2 in figure 5.12a). These new behaviours can be attributed to the nature of the ambient fluid, and are explained by the competition between particle segregation and ambient fluid effects. In fact, the front speed decreases when the particle diameter decreases, and this effect is enhanced in
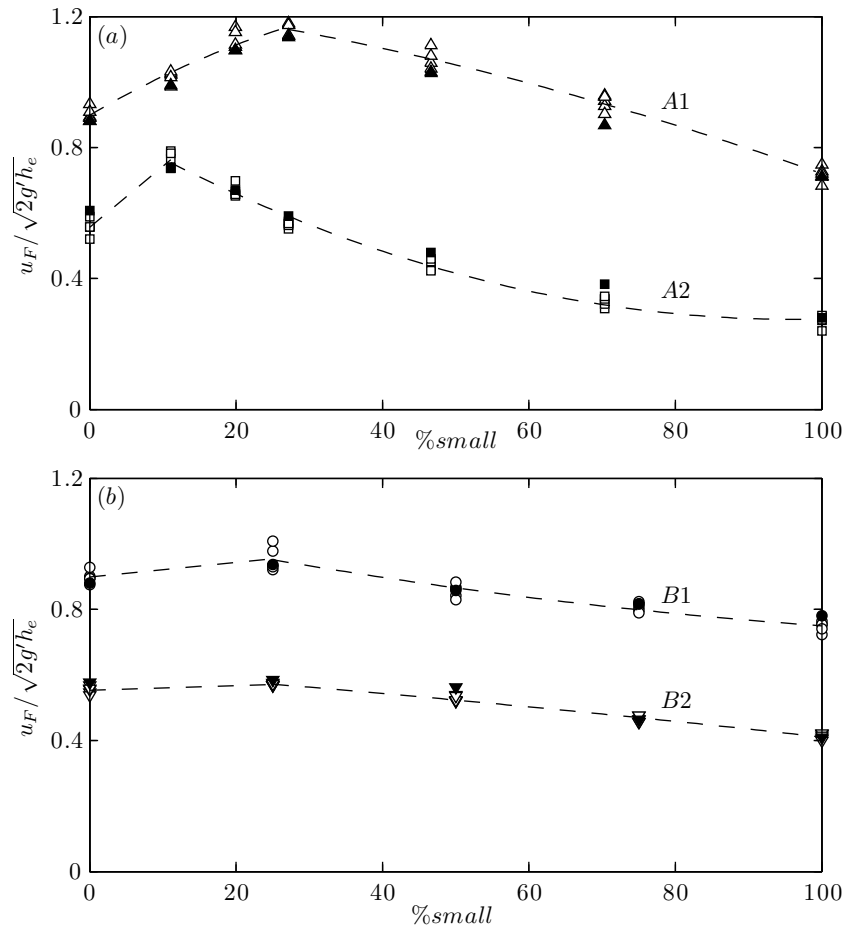
FIGURE 5.12. Froude number $Fr = u_F/\sqrt{2g'h_e}$ as a function of the initial volume fraction of small grains for sets A1 (in air, $\triangle$) and A2 (in water, $\square$) (a), and B1 (in air, $\circ$) and B2 (in water, $\triangledown$) (b) of table 3.2. White marks are experimental measurements with h_o/x_o=2,3,4,6,8; and black marks are simulation results with h_o/x_o=6 and σ=1.4. The experimental tendency is represented by the dashed line.

water (see figure 5.5). This is illustrated in figure 5.13 that presents a comparison of the results for experiments in air (A1.4, left panels of figure 5.13) and in water (A2.4, right panels of figure 5.13). Figures 5.13 (a,b) show the experimental image of the granular flow and figures 5.13 (c,d) show the contour graph of the total solid concentration, while figures 5.13 (e,f) show the dimensionless horizontal fluid velocity and drag force profiles in the front area. It is observed that although in both cases drag forces coupled with wall fluid viscous effects counteract the movement of the solids (see arrows in figures 5.13e and 5.13f), the ambient fluid effects are more important in water than in air (compare arrows in figure 5.13e with arrows in figure 5.13f). Furthermore, figures 5.13 (a,d) show that, in general, there is a good agreement between the experimental and numerical morphologies of the granular flow. Discrepancies are observed, however, in case of ambient water for which experimentally is observed that the particles that
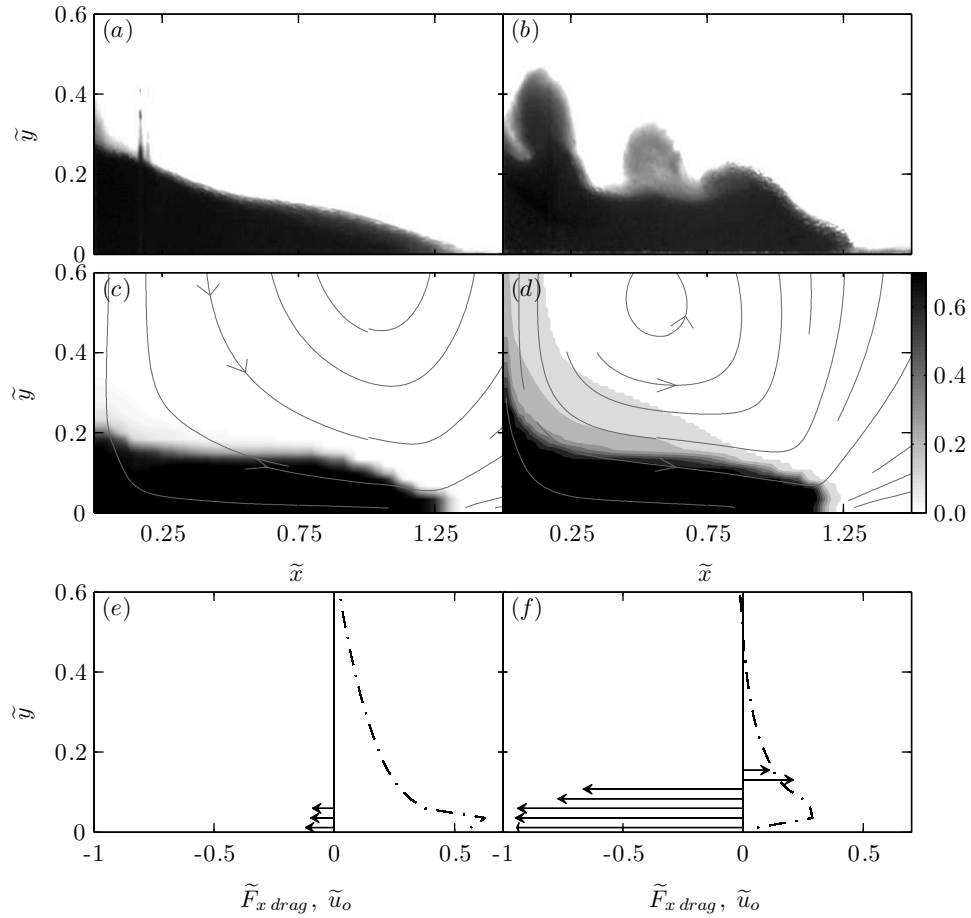
FIGURE 5.13. Results for experiments A1.4 at $\widetilde{t} = 1.9$ (in air, left panels) and A2.4 at $\widetilde{t} = 2.9$ (in water, right panels). (a,b) Experimental image. (c,d) Contour graph of the total solid concentration, $c_1 + c_2$, and the streamlines of fluid velocity $(\rightarrow\!\!\rightarrow)$. (e,f) Dimensionless horizontal fluid velocity, $\widetilde{u}_0$ $(-\cdot-\cdot)$, and drag force, $\widetilde{F}_{x\,drag} = \sum_{\alpha=1}^{2} \sqrt{De\,h_o/(Ar_\alpha\,d_\alpha)} \widetilde{K}_\alpha/c[\widetilde{u}_0 - \widetilde{u}_\alpha]$ $(\rightarrow)$, profiles in the front area.

are in suspension at the top of the granular flow are concentrated in eddies (figure 5.13b), whereas numerically is obtained a smooth region with low concentration of particles (figure 5.13d). This is because the experimental image corresponds to just one realization and the results of the model equations correspond to an average over many realizations (Reynolds (1895) average equations).

Chapter 6

Discussion and conclusions

In this thesis, a theoretical framework based on the mixture theory was developed to study a dense granular flow composed by several solid constituents and a Newtonian ambient fluid. These fully coupled equations have four important characteristics: (i) they consider the compressible nature of a granular flow, (ii) they are able to dynamically create interfaces, (iii) they consider the coupled dynamics between the drag forces and the turbulence of the ambient fluid, and (iv) they consider the feedback that exists between the particle-size distribution and the dynamics of the flow. This continuum framework may be useful to study the large scale dynamics of granular flows such as geophysical flows, which are dense heterogeneous granular flows that are characterized by unsteady and non uniform flow conditions.

6.1. On the role of the ambient fluid on granular flows

The particular dynamics of the collapse and spreading of a two-dimensional granular column in air or water was successfully solved for a wide range of column aspect ratios, $h_o/x_o \in [1, 16]$. A key feature of the governing equations is the representation of the rate-independent quasi-static part of constituent stresses of the solid particles defined by (2.19) and (2.20), which induces the fall of the particles while the flow is not packed, and creates static and dynamic regions during the granular column collapse because of the Mohr-Coulomb condition (figure 5.2). Moreover, the inherent non-hydrostatic feature of the governing equations allows the handling of the reported problem in the shallow water equations for high aspect ratios (e.g. Larrieu *et al.* 2006).

By introducing $h_e = h_e(\tan \varphi, h_o/x_o)$ from numerical experiments without fluid and particles collisions (figure 5.4b), the effects of $\tan \varphi$ and h_o/x_o were subtracted, allowing the analysis of the role of the ambient fluid on gravitational granular flow dynamics. Buoyancy is the direct and simplest consequence of the presence of an ambient fluid; however, experimental measurements cannot be explained if the hydrodynamic fluid pressure and drag interactions are not included in the analysis. In fact, fluid pressure gradient and drag interaction terms in (4.4) are coupled and act on the granular flow dynamics. This is shown in figure 5.5 (b), in which the best fit for the experimental measurements was found with a combination of De and Ar_1, which are dimensionless

numbers that weight the fluid pressure gradient and the drag terms in (4.4) at the laboratory scale considered. The magnitude of the fluid pressure fluctuations at the flow front is described by De, while the magnitude of the momentum transfer by drag interactions is described by Ar_1. The combination of both dimensionless numbers determines the dominant terms that describe the force balance during the constant front velocity regime. In air, the dominant dynamical balance results from solid pressure gradient and Coulomb friction (figure 5.7c), because the hydrodynamic fluid pressure that results from volume interchanges and momentum transfer by drag interactions, is not large enough to support the reduced weight of the solid particles (figure 5.6c). In contrast, in the case of water in which the fluid pressure fluctuations are larger, the local behaviour change to a dense suspension for the smaller particles (d_1 equal to 0.2 and 0.7 mm), because the increase of momentum transfer by drag interactions results in an increase of the hydrodynamic fluid pressure that finally support the reduced weight of the solid particles (figure 5.6d), thus resulting in the dominant dynamical balance described by advection and drag forces (figure 5.7d). Furthermore, in cases of both air and water drag forces coupled with the wall fluid viscous effects counteract the solid movement (figures 5.6e and 5.6f); in this context, fluid turbulence is particularly important and has to be considered in the analysis (figure 5.8), that is, the problem is taken back to fluid turbulence, which is a fundamental issue in fluid mechanics.

As the interaction mechanisms cannot be restricted to buoyancy or volume exchanges, arguments of low fluid density (Campbell 2006) or constant solid bulk density (Hutter *et al.* 2005) are not enough to neglect the ambient fluid effects. For instance, consider the case of a dense granular flow, for which particles collisions can be ignored, immersed in a real fluid with very low material density (*dry dense granular flows*), the equations of motion for the solid phase (2.27) reduce to

$$\frac{\partial \rho_1 u_{1i}}{\partial t} + \frac{\partial (\rho_1 u_{1j} u_{1i})}{\partial x_j} = \rho_1 \frac{g_i}{g} - \frac{\partial p_1}{\partial x_i} + s_{ij} \frac{\partial p_1}{\partial x_j} \tan \varphi. \tag{6.1}$$

Some features of dry dense granular flows can be deduced from these equations. First, the motion depends neither on the fluid phase nor on the solid particle diameter. Second, dry dense granular flows do not reach a uniform steady state flow regime. If this is the case, the left hand side terms of (6.1) as well as the horizontal pressure gradient are zero, resulting in the pressure distribution of the static case. If there is motion, the only way to balance gravity and pressure forces is by flow acceleration. As a consequence, to explain the widely reported uniform steady state flow regime of dry dense granular flows found in different experimental configurations (e.g. GDR MiDi 2004; Forterre & Pouliquen 2008), an additional sink of momentum has to be considered. Although particles collisions may provide the sink of momentum required

to balance gravity and pressure forces, the uniform steady state flow regime for dry dense granular flows can also be explained by drag forces that transfer momentum from solid to fluid phases. This transfer indirectly allows the fluid turbulence to contribute in the solid phase force balance, as fluid turbulence decreases the fluid velocity, thus increasing drag forces that finally counteract the gravity in the solid phase force balance. Furthermore, analyses made by Cassar *et al.* (2005) and Forterre & Pouliquen (2008), without invoking explicitly the ambient fluid effects, indirectly consider drag forces on the falling time scale of the particles used to derive friction laws for uniform steady avalanches. That is, even with ambient air, the fluid effects that are commonly ignored could become strong enough to explain, for instance, the uniform steady state flow regime.

We conclude that the effects of the ambient fluid on the dynamics of granular flows cannot be neglected. This means that in order to properly describe the granular flow dynamics, a two-phase approach has to be used. This is because conceptually the effects of the ambient fluid represent an interaction force in the solid phase momentum equations, so that they cannot be incorporated in the stress tensor of the solid phase. The advantage of separating solid and fluid phases is that when studying the solid phase, the set of material properties that control the flow behaviour can be identified, thus enabling to look for a general constitutive law to represent the stress tensor of the solid phase for any granular flow regime.

6.2. On the dynamics of dense heterogeneous granular flows

Once the ambient fluid effects were identified, we analysed the dynamics of dense heterogeneous granular flows. In particular, we proposed a new constitutive relation (2.38) that describes the interaction mechanisms between the solid species in a dense regime. Our results suggest that the model equations include the essential features that describe the dynamics of dense heterogenous granular flows (figure 5.11). The key feature of the model equations is the new constitutive relation of (2.38), which correctly represents the interactions between solid species in a dense regime, since one species can be split into two sub-constituents and the resulting dynamics is independent of that subdivision (figure 5.9). With this new constitutive relation, the effect of difference in diameter between two solid constituents is only taken into account in the model through the interactions with the ambient fluid (2.39); however, the dynamics of dense heterogeneous granular flows is incomplete unless the kinetic sieving of small grains is included (figure 5.10a). For doing this, the empirical function of (2.53) was introduced to represent the fact that under a critical value of the mixture concentration, only small particles fall down while large particles remain packed (Savage & Lun 1988). The

direct effect of (2.53) was the segregation of the constituents (compare figures 5.10c and 5.10d), which can be explained using the squeeze expulsion mechanism described by Savage & Lun (1988) and later by Pouliquen & Vallance (1999) and Gray & Thornton (2005). This squeeze mechanism is based on the fact that percolation of small grains produces force imbalances at the base of the flow, thus forcing the large particles to move upward and leading to vertical segregation. This squeeze expulsion mechanism was a natural result of the model (figure 5.10c), which validates the experimental hypothesis of (2.53), since both front speed and final deposit fit relatively well with the laboratory measurements (figures 5.10 and 5.11).

An important consequence of the segregation of the granular flow is the increase of the solids mixture volume because of the decrease of the mixture concentration (see figure 2.2), which is then reflected in an increase in both the runout distance and the front speed (figure 5.10). The increase in front speed is explained in terms of the kinetic energy of the flow, which is proportional to both solid concentration and square velocity, then a decrease in solid concentration is compensated with an increase in speed (see curves A1 and B1 of figure 5.12). This increase in flow mobility when adding a small amount of small grains has been reported in experiments (Roche *et al.* 2005; Phillips *et al.* 2006) and in soft particle discrete element numerical simulations (Linares-Gerrero *et al.* 2007), but using as a control parameter the ratio of the runout distance to the fall height. In these studies the increase of mobility has been attributed to a thin layer of small particles that may change the frictional dynamics at the base of the flow (Phillips *et al.* 2006; Linares-Gerrero *et al.* 2007); however, the results of figure 5.10 suggest that the volumetric expansion of the flow caused by the particle segregation is enough to explain the enhanced mobility. This segregation effect may be in contradiction with Phillips *et al.* (2006) who found that a deposit of a granular flow with high mobility appears to have less segregation than a deposit of a flow with low mobility; however, they agree with us in the fact that the maximum flow mobility is obtained for initial mixture concentrations close to the maximum packing concentration ($\sim 27\%$ of fraction of small grains, see curves A1 and B1 of figure 5.12), for which the increase in mixture volume due to segregation is greater (see figure 2.2). This is also in agreement with Roche *et al.* (2005) and Linares-Gerrero *et al.* (2007) who showed that the runout distance is greater for initial mixture concentrations close to the optimal packing. Then, although the increase in front speed may be the result of both the expansion of the granular flow and the lubrication at the base of the flow, the expansion of the flow due to particle segregation appears to be the main mechanism that explains this behaviour. So far, this volumetric expansion of the flow due to particle segregation has not been investigated before and further experimental analysis is required to validate our hypothesis.

Furthermore, we showed that because of the ambient fluid effects, small grains are more resistant to flow than large grains, so that the front speed decreases when the grain size decreases, and this behaviour is even more pronounced in water compared to the case in air (see figure 5.5). In the context of the three-species granular flows analysed here, these ambient fluid effects allow to explain the results of figure 5.12, which shows that the increase in flow speed due to the volumetric expansion is damped in water compared to the case in air (compare experiments A1 and A2 in figure 5.12a). As discussed, this occurred because the drag forces coupled with the wall fluid viscous effects counteract the movement of the solid particles (figures 5.13e and 5.13f). Therefore, although a mixture of small and large grains may segregate and the front speed may increase, drag forces counteract the movement of the solids, thus competing with segregation. In this context, it would be interesting to investigate if such a relation is encountered in geophysical flows such as landslides and debris avalanches.

Appendix: Numerical scheme

Each of the governing equations can be written in the general convection-diffusion transport equation with source terms:

$$\frac{\partial \rho \phi}{\partial t} + \frac{\partial (\rho u_j \phi)}{\partial x_j} = \frac{\partial}{\partial x_j}\left(\Gamma \frac{\partial \phi}{\partial x_j}\right) + S, \tag{A.1}$$

where ρ is the density, ϕ is the dependent variable, Γ is the diffusion coefficient, and S is the source term. The particular representation of each term in the context of the governing equations (2.45)-(2.46) and (2.47)-(2.49) is listed in table A.4.

Following Patankar (1980), each governing equation was discretised using both the hybrid scheme (Patankar 1980, pp. 88–90) and the linearisation procedure for the source terms (Patankar 1980, pp. 48–49). The final two-dimensional discretisation equation is written generically as

$$
\begin{aligned}
&a_P \phi_P = a_E \phi_E + a_W \phi_W + a_N \phi_N + a_S \phi_S + b, \\
&a_E = \|-F_e, D_e - F_e/2, 0\|, \ a_W = \|F_w, D_w + F_w/2, 0\|, \\
&a_N = \|-F_n, D_n - F_n/2, 0\|, \ a_S = \|F_s, D_s + F_s/2, 0\|, \\
&a_P = a_E + a_W + a_N + a_S + a_P^o - S_P \Delta x \Delta y + (F_e - F_w) + (F_n - F_s), \\
&a_P^o = \rho_P^o \Delta x \Delta y / \Delta t, \ b = S_C \Delta x \Delta y + a_P^o \phi_P^o,
\end{aligned}
\tag{A.2}
$$

where the sub-index with the upper-case letter $k = E, W, N, S$ refers to the quantities evaluated at the node east, west, north, south of the central node P; the sub-index with the lower-case letter $l = e, w, n, s$ refers to the quantities evaluated on the face east, west, north, south of the control volume P; the upper-index $()^o$ refers to the value of the quantities evaluated in the previous time step; $\| \ \|$ stands for the largest of the quantities within it; S_C and S_P arise from the linearization of the source term $S = S_P \phi_P + S_C$; and the convective, F_l, and diffusive, D_l, fluxes are

$$
\begin{aligned}
&F_e = (\rho u)_e \Delta y, \ F_w = (\rho u)_w \Delta y, \ F_n = (\rho u)_n \Delta x, \ F_s = (\rho u)_s \Delta x, \\
&D_e = \Gamma_e \Delta y / \Delta x, \ D_w = \Gamma_w \Delta y / \Delta x, \ D_n = \Gamma_n \Delta x / \Delta y, \ D_s = \Gamma_s \Delta x / \Delta y.
\end{aligned}
\tag{A.3}
$$

Note that the source terms of the discretised momentum equations (2.47) and (2.48) contain the pressure that is unknown (table A.4), so that the mass continuity equations have to be included in order to close the system of equations. For doing this, we followed the iterative SIMPLE (Semi-Implicit Method for Pressure-Linked Equations) algorithm explained in detail in Chapter 6 of Patankar (1980). In this methodology, the pressure and velocities are written as

$$p = p^* + p', \ u = u^* + u', \ v = v^* + v', \tag{A.4}$$

Equation	ρ	ϕ	Γ	S
(2.45)	ρ_0	k	μ_T/σ_k	$\mu_T(\partial_{x_j}u_{0i}+\partial_{x_i}u_{0j})\partial_{x_j}u_{0i}+\sum_{\beta=1}^{N}K_\beta|\boldsymbol{u}_0-\boldsymbol{u}_\beta|^2-\rho_0\epsilon$
(2.46)	ρ_0	ϵ	μ_T/σ_ϵ	$c_{1\epsilon}\epsilon/k[\mu_T(\partial_{x_j}u_{0i}+\partial_{x_i}u_{0j})\partial_{x_j}u_{0i}+\sum_{\beta=1}^{N}K_\beta|\boldsymbol{u}_0-\boldsymbol{u}_\beta|^2]-c_{2\epsilon}\rho_0\epsilon^2/k$
(2.47)	γ_α	c_α	-	-
(2.48)	ρ_0	u_{0i}	$\mu_0+\mu_T$	$\rho_0 g_i - c_0\partial_{x_i}p_0 - \sum_{\beta=1}^{N}K_\beta(u_{0i}-u_{\beta i})$
(2.49)	ρ_α	$u_{\alpha i}$	-	$\rho_\alpha g_i - \partial p_\alpha/\partial x_i + s_{\alpha ij}\partial p_\alpha/\partial x_j\tan\varphi_\alpha + \hat{m}_{\alpha i}$

TABLE A.4. Particular representation of the density, ρ, the dependent variable, ϕ, the diffusion coefficient, Γ, and the source term, S, for each equation.

where $()^*$ denotes guessed values (or values of the previous iteration) and $()'$ denotes correction values. Using p^*, the velocities u^* and v^* are obtained by solving the momentum equations. Then, the correction for the pressure p' is obtained from the pressure-correction equation given by (Patankar 1980, pp. 124–126),

$$
\begin{aligned}
&a_P p'_P = a_E p'_E + a_W p'_W + a_N p'_N + a_S p'_S + b, \\
&a_E = \rho_e d_e \Delta y, \ a_W = \rho_w d_w \Delta y, \ a_N = \rho_n d_n \Delta x, \ a_S = \rho_s d_s \Delta x, \\
&d_e = \Delta y/a_e^u, \ d_w = \Delta y/a_w^u, \ d_n = \Delta x/a_n^v, \ d_s = \Delta x/a_s^v, \\
&a_P = a_E + a_W + a_N + a_S, \\
&b = (\rho_P^o - \rho_P)\Delta x \Delta y/\Delta t + (F_w - F_e) + (F_s - F_n),
\end{aligned}
\tag{A.5}
$$

where a_e^u, a_w^u and a_n^v, a_s^v are the corresponding coefficients that comes from the u and v momentum equation that are discretised in the east, west, and north, south faces of the control volume for the pressure equation. Finally, the corrections for the velocities, u' and v', are computed with (Patankar 1980, pp. 124–126)

$$
u'_e = d_e(p'_P - p'_E), \ u'_w = d_w(p'_W - p'_E), \ v'_n = d_n(p'_P - p'_N), \ v'_s = d_s(p'_S - p'_P). \tag{A.6}
$$

Note also that this procedure is applied to each constituent separately, and in the case of the solids momentum equations (2.48), the inclusion of the solid pressure closure (2.28) implies that the pressure-correction equation is applied only at points where the flow is packed, that is, at points in which the flow is incompressible.

Finally, it is important to mention that for solving the convection-diffusion equation two kinds of boundary conditions can be chosen: a given boundary value or a given boundary flux. As the momentum equations are a particular case of this general equation, the same boundary condition treatment applies to them as well. The only difference is that for the pressure-correction equation an additional condition at the boundary has to be given, which could be the pressure at the boundary (and the normal velocity is then unknown) or the normal velocity at the boundary (and the pressure is then unknown) (Patankar 1980, pp. 129–130).

Bibliography

ANCEY, C. 2007 Plasticity and geophysical flows: A review. *J. Non-Newtonian Fluid Mech.* **142**, 4–35.

ANDERSON, T.B. & JACKSON, R. 1967 A fluid mechanical description of fluidized beds: equations of motion. *Ind. Eng. Chem. Fundam.* **6**, 527–539.

BAGNOLD, R.A. 1954 Experiments on a gravity-free dispersion of large solid spheres in a newtonian fluid under shear. *Proc. R. Soc. London Ser. A* **225**, 49–63.

BALMFORTH, N.J. & KERSWELL, R.R. 2005 Granular collapse in two dimensions. *J. Fluid Mech.* **538**, 399–428.

BEDFORD, A. 1983 Recent advances: theories of immiscible and structured mixtures. *Int. J. Engng Sci.* **21**, 863–960.

BISWAS, P., SANCHEZ, P., SWIFT, M. & KING, P. 2003 Numerical simulations of air-driven granular separion. *Phys. Rev. E* **68**, 050301.

BOUSSINESQ, J. 1877 Théorie de l'écoulement tourbillant. *Mem. Présentés par Divers Savants Acad. Sci. Inst. Fr.* **23**, 46–50.

BURTALLY, N., KING, P. J. & SWIFT, M. R. 2002 Spontaneous air-driven separation in vertically vibrated fine granular mixtures. *Science* **295**, 1877–1879.

CAMPBELL, C. 1990 Rapid granular flows. *Annu. Rev. Fluid Mech.* **22**, 57–92.

CAMPBELL, C. 2006 Granular material flows - an overview. *Powder Technol.* **162**, 208–229.

CASSAR, C., NICOLAS, M. & POULIQUEN, O. 2005 Submarine granular flows down inclined planes. *Phys. Fluids* **17**, 103301.

CLAVERO, J.E., SPARKS, R.S.J., HUPPERT, H.E. & DADE, W.B. 2002 Geological constraints on the emplacement mechanism of the parinacota debris avalanche, northern chile. *Bull Volcanol* **64**, 40–54.

CROWE, C.T. 2000 On models for turbulence modulation in fluid-particle flows. *Int. J. Multiphase Flow* **26**, 719–727.

CROWE, C.T., TROUTT, R. & CHUNG, J.N. 1996 Numerical models for two-phase turbulent flows. *Annu. Rev. Fluid. Mech.* **28**, 11–43.

CUNDALL, P.A. & STRACK, O.D.L. 1979 A discrete numerical model for granular assemblies. *Geotechnique* **29**, 47–65.

DALLAVALLE, J.M. 1948 *Micromeritics: the technology of fine particles*. 2nd Edition Pitman, London.

DI FELICE, R. 1994 The voidage function for fluid-particle interaction systems. *Int. J. Multiphase Flow* **20**, 153–159.

Di Felice, R. 1995 Hydrodynamics of liquid fluidisation. *Chem. Eng. Sci.* **50**, 1213–1245.

Dolgunin, V. & Ukolov, A. 1995 Segregation modeling of particle rapid gravity flow. *Powder Technol.* **83**, 95–103.

Drew, D.A. 1983 Mathematical modelling of two-phase flow. *Annu. Rev. Fluid Mech.* **15**, 261–291.

Elghobashi, S. & Truesdell, G.C. 1993 On the two-way interaction between homogeneous turbulence and dispersed solid particles. ii: Turbulence modification. *Phys. Fluids* **5**, 1790–1801.

Fedors, R.F. & Landel, R.F. 1979 An empirical method of estimating the void fraction in mixtures of uniform particles of different size. *Powder Technol.* **23**, 225–231.

Forterre, Y. & Pouliquen, O. 2008 Flows of dense granular media. *Annu. Rev. Fluid Mech.* **40**, 1–24.

German, R.M. 1989 *Particle packing characteristics*. Metal Powder Industries Federation, Princeton, N.J.

Goldhirsch, I. 2003 Rapid granular flows. *Annu. Rev. Fluid Mech.* **35**, 267–293.

Goodman, M. & Cowin, S. 1971 Two problems in the gravity flow of granular materials. *J. Fluid Mech.* **45**, 321–339.

Gray, J. & Thornton, A. 2005 A theory for particle size segregation in shallow granular free-surface ows. *Proc. R. Soc. A* **461**, 1447–1473.

Gray, J. M. N. T. & Ancey, Ch. 2009 Segregation, recirculation and deposition of coarse particles near two-dimensional avalance fronts. *J. Fluid Mech.* **629**, 387–423.

Gray, J. M. N. T. & Chugunov, V. A. 2006 Particle-size segregation and diffusive remixing in shallow granular avalanches. *J. Fluid Mech.* **569**, 365–398.

Hutter, K., Wang, Y. & Pudasaini, S. 2005 The savage-hutter avalanche model. how far can it be pushed? *Phil. Trans. R. Soc. A* **363**, 1507–1528.

Ippolito, I., Samsom, L., Bourles, S. & Hulin, J. 2000 Diffusion of a single particle in a 3d random packing of spheres. *Eur. Phys. J. E* **3**, 227–236.

Iverson, R. 1997 The physics of debris flows. *Rev. Geophys.* **35**, 245–296.

Iverson, R. & Denlinger, R. 2001 Flow of variably fludized granular masses across three-dimensional terrain 1. coulomb mixture theory. *J. Geophys. Res.* **106**, 537–552.

Jackson, R. 2000 *The dynamics of fluidized particles*. Cambridge University Press.

Jenkins, J.T. & Savage, S.B. 1983 A theory for the rapid flow of identical, smooth, nearly elastic, spherical particles. *J. Fluid Mech.* **130**, 187–202.

Johnson, P.C. & Jackson, R. 1987 Frictional-collisional constitutive relations for granular materials, with application to plane shearing. *J. Fluid Mech.* **176**, 67–93.

Joseph, D. & Lundgren, T. 1990 Ensemble averaged and mixture theory equations for incompressible fluid-particle suspensions. *Int. J. Multiphase Flow* **16**, 35–42.

von Karman, T. 1940 The engineer grapples with nonlinear problems. *Bull. Am. Math. Soc.* **46**, 615–683.

Lajeunesse, E., Monnier, J. & Homsy, G. 2005 Granular slumping on a horizontal surface. *Phys. Fluids* **17**, 103302.

Larrieu, E., Staron, L. & Hinch, E. 2006 Raining into shallow water as a description of the collapse of a column of grains. *J. Fluid Mech.* **554**, 259–270.

Linares-Gerrero, E., Goujon, C. & Zenit, R. 2007 Increased mobility of bidisperse granular avalanches. *J. Fluid Mech.* **593**, 475–504.

Lube, G., Huppert, H., Sparks, R. & Freundt, A. 2005 Collapses of two-dimensional granular columns. *Phys. Rev. E* **72**, 041301.

Lun, C.K.K., Savage, B. & Jeffrey, D.J. 1984 Kinetic theories for granular flow: inelastic particles in couette flow and slightly inelastic particles in a general flow field. *J. Fluid Mech.* **140**, 223–256.

Makse, H. A., Havlin, S., King, P. R. & Stanley, E. 1997 Spontaneous stratification in granular mixtures. *Nature* **386**, 379–382.

Meruane, C., Tamburrino, A. & Roche, O. 2010 On the role of the ambient fluid on gravitational granular flow dynamics. *J. Fluid Mech.* **648**, 381–404.

MiDi, GDR 2004 On dense granular flows. *Eur. Phys. J. E* **14**, 341–365.

Moreau, J. 1994 Some numerical methods in multibody dynamics: Application to granular materials. *Eur. J. Mech. A* **4**, 93–114.

Morland, L.W. 1992 Flow of viscous fluids through a porous deformable matrix. *Surv. Geophys.* **13**, 209–268.

Morland, L. & Sellers, S. 2001 Multiphase mixtures and singular surfaces. *Int. J. Non Linear Mech.* **36**, 131–146.

Ottino, J. & Khakhar, D. 2000 Mixing and segregation of granular materials. *Annu. Rev. Fluid Mech.* **32**, 55–91.

Passman, S.L., Nunziato, J.W. & Walsh, E.K. 1984 *A theory of multiphase mixtures*. Appendix 5C in: C. Truesdell (*eds*) Rational thermodynamics, Springer-Verlag, p. 286-325.

Patankar, S.V. 1980 *Numerical heat transfer and fluid flow*. Hemisphere Publising Corporation, Taylor and Francis Group. New York.

Pelanti, M., Bouchut, F. & Mangeney, A. 2008 A roe-type scheme for two-

phase shallow granular flows over variable topography. *ESAIM: M2ANESAIM: M2AN* **42**, 851–885.

Phillips, J., Hogg, A., Kerswell, R. & Thomas, N. 2006 Enhanced mobility of granular mixtures of fine and coarse particles. *Earth Planet. Sci. Lett.* **246**, 466–480.

Pitman, B. & Le, L. 2005 A two-fluid model for avalanche and debris flows. *Phil. Trans. R. Soc. A* **363**, 1573–1601.

Pope, S. 2000 *Turbulent flows*. Cambridge University Press.

Pouliquen, O., Delour, J. & Savage, S. B. 1997 Fingering in granular flows. *Nature* **386**, 816–817.

Pouliquen, O. & Vallance, J. 1999 Segregation induced instabilities of granular fronts. *Chaos* **9**, 621–631.

Pudasaini, S., Wang, Y. & Hutter, K. 2005 Rapid motions of free-surface avalanches down curved and twisted channels and their numerical simulation. *Phil. Trans. R. Soc. A* **363**, 1551–1571.

Reynolds, O. 1895 On the dynamical theory of turbulent incompressible viscous fluids and the determination of the criterion. *Phil. Trans. R. Soc. A* **186**, 121–161.

Roche, O., Gilbertson, M., Phillips, J. & Sparks, R. 2005 Inviscid behaviour of fines-rich pyroclastic flows inferred from experiments on gas–particle mixtures. *Earth Planet. Sci. Lett.* **240**, 401–414.

Rodi, W. 1983 *Turbulence models and their application in hydraulics - A state-of-the-art review*. IAHR.

Rutgers, R. 1962 Packing of spheres. *Nature* **193**, 465–466.

Savage, S.B. 1983 *Granular flows down rough inclines - review and extension*. In Jenkins, J.T. and Satake, M. (*eds*) Mechanical of granular materials: New models and constitutive relations, Elsevier, p. 261 - 282.

Savage, S. & Huter, K. 1989 The motion of finite mass of granular material down a rough incline. *J. Fluid Mech.* **199**, 177–215.

Savage, S. B. & Lun, C. K. K. 1988 Particle size segregation in inclined chute flow of dry cohesionless granular solids. *J. Fluid Mech.* **189**, 311–335.

Staron, L. & Hinch, E.J. 2005 Study of the collapse of granular columns using two-dimensional discrete-grain simulation. *J. Fluid Mech.* **545**, 1–27.

Stewart, H.B. & Wendroff, B. 1984 Two-phase flow: models and methods. *J. Comput. Phys.* **56**, 363–409.

Sundaresan, S. 2003 Instabilities in fluidized beds. *Annu. Rev. Fluid Mech.* **35**, 63–88.

Thomas, N. 2000 Reverse and intermediate segragation of large beads in dry granular media. *Phys. Rev. E* **62**, 961–974.

THORNTON, A., GRAY, J. & HOGG, A. 2006 A three-phase mixture theory for particle size segregation in shallow granular free-surface ows. *J. Fluid Mech.* **550**, 1–25.

TRUESDELL, C. 1957 Sulle basi della thermomecanica. *Rand Lincei, Ser.* **8**, 33–38.

TRUESDELL, C. 1984 *Rational thermodynamics*. Springer-Verlag.

VALLANCE, J. & SAVAGE, S. B. 2000 Particle segregation in granular flows down chutes. In *IUTAM symposium on segregation in granular materials* (ed. A. Rosato & D. Blackmore), pp. 31–51.

VAN WYK DE VRIES, B., SELF, S., FRANCIS, P.W. & KESZTHELY, L. 2001 A gravitational spreading origin for the socompa debris avalanche. *Journal of Volcanology and Geothermal Research* **105**, 225–247.

WANG, Y. & HUTTER, K. 2001 *Granular material theories revisited*. Chapter 04 in: N.J. Balmforth and A. Provenzale (*eds*) Geomorphological fluid mechanics, Springer, p. 79-107.

WIELAND, M., GRAY, J.M.T. & HUTER, K. 1999 Channelized free-surface flow of cohesionless granular avalanches in a chute with shallow lateral curvature. *J. Fluid Mech.* **392**, 73–100.

YSTROM, J. 2001 On two-fluid equations for dispersed incompressible two-phase flow. *Comput. Visual. Sci.* **4**, 125–135.

Continuum equations for studying the dynamics of dense heterogeneous granular flows

Carolina MERUANE

Summary

Most dense grains flows in nature, such as debris avalanches, pyroclastic flows, and subaquatic avalanches, involve a wide range of different solid constituents that are immersed in an ambient fluid. In order to obtain a good representation of these flows, the interaction mechanisms among the different constituents of the mixture should be considered. In this research, it was developed a theoretical framework based on the mixture theory for representing the dynamics of a dense heterogeneous granular flow composed by a number of solid species with different properties, and immersed in a Newtonian ambient fluid. These fully coupled equations were solved numerically and validated by comparing the numerical results with experimental measurements of gravitational granular flows, triggered by the collapse of two-dimensional granular columns in ambient air or water. This theory was then used to investigate the ambient fluid effects on homogeneous granular flow dynamics, and the segregation effects on the dynamics of binary mixtures of small and large spherical particles of equal mass density. Our results suggest that the model equations include the essential features that describe the dynamics of dense heterogeneous granular flows. In particular, it is shown that segregation of the granular material increases the front speed because of the volumetric expansion of the flow. This increase in flow speed is damped by the ambient fluid, and this behavior is more pronounced in water compared to the case in air. It is concluded that a realistic model of dense heterogeneous granular flows should consider at least three constituents: large and small grains, and the ambient fluid.

Equations continues pour l'étude de la dynamique des écoulements granulaires denses hétérogènes

Carolina MERUANE

Résumé

La plupart des écoulements granulaires denses dans la nature, tels que les avalanches de débris, les écoulements pyroclastiques et les avalanches sous-marines, sont constitués d'un large éventail de différents composants solides immergés dans un environnement fluide. Afin d'obtenir une bonne représentation de la dynamique de ces écoulements, il est nécessaire d'examiner les mécanismes d'interaction entre les différents composants du mélange. Dans ce travail, nous avons développé un cadre théorique basé sur la théorie de mélange afin de représenter la dynamique d'un écoulement dense de matériau granulaire hétérogène composé d'un certain nombre d'espèces solides avec des propriétés différentes, et immergé dans un environnement fluide Newtonien. Le système d'équations obtenu a été validé en comparant les résultats numériques avec des mesures expérimentales obtenues pour des écoulements gravitaires de matériaux granulaires, générés par l'effondrement d'une colonne de grains en deux dimensions, en utilisant de l'air ou de l'eau comme milieu fluide. Cette théorie a ensuite été utilisée pour étudier les effets du fluide ambiant sur la dynamique des écoulements de matériaux granulaires homogènes, ainsi que les effets de la ségrégation sur la dynamique des écoulements granulaires de mélanges binaires constitués de petites et grandes particules sphériques d'égale densité. Nos résultats suggèrent que les équations reproduisent les caractéristiques essentielles de la dynamique des écoulements granulaires denses hétérogènes. En particulier, nous démontrons que la ségrégation des matériaux granulaires augmente la vitesse du front en raison de la dilatation de l'écoulement. Cette augmentation de la vitesse d'écoulement est amortie par l'environnement fluide, et ce comportement est plus marqué dans l'eau que dans l'air. Nous concluons qu'un modèle réaliste pour des écoulements granulaires hétérogènes doit considérer au moins trois éléments: des grains de petite et de grande taille et un environnement fluide.